Editors' Suggestion | Featured in Physics

$^{19}F(p,\gamma)^{20}Ne$ and $^{19}F(p,\alpha)^{16}O$ reaction rates and their effect on calcium production in Population III stars from hot CNO breakout

R. J. deBoer,[1,*] O. Clarkson,[2,3,4] A. J. Couture,[5] J. Görres,[1] F. Herwig,[2,3,4] I. Lombardo,[6] P. Scholz,[1] and M. Wiescher[1]

[1]*The Joint Institute for Nuclear Astrophysics, Department of Physics, University of Notre Dame, Notre Dame, Indiana 46556, USA*
[2]*Department of Physics & Astronomy, University of Victoria, Victoria, BC V8W 2Y2, Canada*
[3]*Joint Institute for Nuclear Astrophysics, Center for the Evolution of the Elements, Michigan State University, East Lansing, Michigan 48824, USA*
[4]*NuGrid Collaboration*
[5]*Los Alamos National Laboratory, Los Alamos, New Mexico 87545, USA*
[6]*INFN, Sezione di Catania, Via Santa Sofia 64, I-95123 Catania, Italy*

(Received 5 January 2021; accepted 9 April 2021; published 26 May 2021; corrected 1 June 2021)

First generation, or Population III, stars have a different evolution than those of later generations owing to their initial primordial abundance composition. Most notably, the lack of carbon, oxygen, and nitrogen means that primordial massive stars must rely on the less efficient *p-p* chains, thereby requiring the star to contract to reach temperatures high enough to eventually trigger 3α reactions. Even small amounts of the $^{12}C(\alpha,\gamma)^{16}O$ reactions begin feeding the CNO mass range and enable the CNO cycle to generate energy, but this occurs at higher temperature compared to later stellar generations. It is currently controversial if the observed enhanced abundances of Ca in the most metal-poor stars could be a result of the high temperature H-burning conditions in the first massive stars. The level of this enrichment depends on the hot breakout path from the CNO cycles via the $^{19}F(p,\gamma)^{20}Ne$ reaction. In this work, the rates of both the $^{19}F(p,\gamma)^{20}Ne$ and competing $^{19}F(p,\alpha)^{16}O$ reactions are re-evaluated using the phenomenological *R*-matrix approach, simultaneously considering several $^{19}F(p,\gamma)^{20}Ne$, $^{19}F(p,\alpha)^{16}O$, and $^{19}F(p,p)^{19}F$ data sets, to better characterize the rate uncertainties. It is found that the rate uncertainty for $^{19}F(p,\gamma)^{20}Ne$ reaction is considerably larger than previously reported. This is the result of undetermined interferences between observed resonances, a possible threshold state, possible subthreshold states, direct capture, and background levels. Additional experimental measurements are therefore needed to determine if $^{19}F(p,\gamma)^{20}Ne$ CNO breakout is responsible for Ca enrichment in metal-poor stars. Astrophysically, the breakout reaction revision makes it less likely that Ca observed in the most Fe-poor stars can originate in hot CNO breakout H-burning nucleosynthtesis, thereby casting doubt on the prevailing faint supernova scenario to explain the abundances observed in these stars.

DOI: 10.1103/PhysRevC.103.055815

I. INTRODUCTION

A fundamental question in nuclear astrophysics concerns the reaction flow out of the CNO cycles toward heavier masses in hydrogen burning environments. At low-temperature hydrogen burning, such as in massive main sequence stars, and even in low-temperature cataclysmic events, such as in classical novae, the CNO matter remains in the mass range below $A \approx 20$. The initial abundance distribution of the CNO isotopes change depending on the temperature density regime of the nucleosynthesis event. Only in explosive hydrogen at burning temperatures sufficiently in excess of ≈0.3 GK, can breakout from the CNO cycles occur via the $^{15}O(\alpha,\gamma)^{19}Ne$ and $^{18}Ne(\alpha,p)^{21}Na$ reactions, triggering a thermonuclear runaway via the αp process. The required temperatures for breakout are anticipated for accreting neutron stars, triggering an x-ray burst as an observable event and are also possible for high temperature nova events associated with accreting white dwarfs. A summary of these breakout scenarios has been discussed before by Wiescher *et al.* [1] and multiple experiments, using a wide range of experimental techniques, have been performed to determine the reaction rates of the α induced breakout reactions $^{15}O(\alpha,\gamma)^{19}Ne$ [2–7] and $^{18}Ne(\alpha,p)^{21}Na$ [8–12].

Little attention has been given to the $^{19}F(p,\gamma)^{20}Ne$ reaction as a possible link between the CNO cycles, the Ne-Na cycles, and possibly beyond. In particular, at temperatures typical for hydrogen-core or -shell burning in massive main-sequence stars, more investigations are needed. In stars with near solar metallicity, the contribution of this reaction to the production of more massive nuclei is negligible compared to other nuclear production mechanisms. However, hot CNO breakout may play a key role in explaining the observed Ca abundance in the most metal-poor stars that carry the abundance signature from the first massive stars.

The most iron-poor stars we observe in our Milky Way's halo are each believed to display the nucleosynthetic

*rdeboer1@nd.edu

signatures resulting from a single Population III (Pop III) star [13]. Keller *et al.* [14] suggested hot CNO breakout during hydrogen burning as the source of Ca production in the most iron and Ca-poor star known at the time, SMSS0313-6708. The Ca abundance was reported as [Ca/H] = −7.2 and −6.94 in analysis done by Nordlander *et al.* [15] using solar abundances of Asplund *et al.* [16]. Takahashi *et al.* [17] also cite hot CNO breakout to produce Ca in SMSS0313-6708, HE 1327-2326, and HE 0107-5240. HE 1327-2326 and HE 0107-5240 have [Ca/H] values of −5.3 and −5.13, respectively, based on an analysis provided in Collet *et al.* [18], and the same solar composition as above.

Using a combination of stellar evolution and single-zone nucleosynthesis calculations, Clarkson and Herwig [19] identified the $^{19}\mathrm{F}(p,\gamma)^{20}\mathrm{Ne}$ reaction as the most important breakout path for hydrogen burning conditions in massive Pop III stars. Clarkson and Herwig [19] investigated the conditions for the hot CNO breakout to produce the observed levels of Ca based on a detailed survey of Pop III massive star simulations with masses ranging from 15 to 140 $\mathrm{M}_{\odot}$, and a range of commonly adopted assumptions on stellar mixing to cover the related systematic uncertainties. They conclude, based on these simulations, that it is unlikely that large amounts of Ca can be produced by hot CNO breakout. Even under the most optimistic assumptions of the mixing and ejection mechanisms, the predicted Ca abundance is between ≈0.8 and nearly 2 dex lower than required by observations of the most metal-poor stars. However, they also note that if the $^{19}\mathrm{F}(p,\gamma)^{20}\mathrm{Ne}/^{19}\mathrm{F}(p,\alpha)^{16}\mathrm{O}$ reaction rate ratio were a factor of ≈10 higher than that reported in the NACRE compilation [20], the model predictions of hot H burning may be able to account for the observed Ca abundances in metal-poor stars.

Based on the presently available nuclear data, the findings of Clarkson and Herwig [19] are in conflict with the previous assertions that the observed Ca in the most metal-poor stars originates in H burning. The question has far-reaching consequences for how the first stars are believed to evolve and die. If Ca can be produced from H burning, then Ca produced in the later Si-burning phases can fall back into the supernova, which is a key ingredient in the prevailing faint supernova with efficient fallback scenario. If Ca cannot be produced in hot H burning, then a new mechanism is needed. Either the supernova scenario has to be revised, or an alternative source must be validated. Other potential sources include a convective-reactive light Pop III *i*-process [21] or Ca synthesis from explosive burning.

As described in Wiescher *et al.* [1], the possibility of a breakout from the cold CNO cycles depends on the feeding of $^{19}\mathrm{F}$ from the equilibrium abundances of $^{17}\mathrm{O}$ and $^{18}\mathrm{O}$ in the third cycle. Leakage via the $^{19}\mathrm{F}(p,\gamma)^{20}\mathrm{Ne}$ reaction would cause an irreversible flow from the CNO to the Ne–Na range because back-processing via $^{22}\mathrm{Ne}(p,\alpha)^{19}\mathrm{F}$ is energetically impossible. The leakage not only depends on the abundance of $^{19}\mathrm{F}$ but also on the reaction rates of $^{19}\mathrm{F}(p,\gamma)^{20}\mathrm{Ne}$ and the competing back-processing reaction $^{19}\mathrm{F}(p,\alpha)^{16}\mathrm{O}$. Therefore, the ratio of the $^{19}\mathrm{F}+p$ reactions is also of critical importance in understanding the production of Ca in the second generation stars observed today.

The compound nucleus of both reactions, $^{20}\mathrm{Ne}$, is characterized by a pronounced α cluster structure [22], which favors the α emission of the $^{19}\mathrm{F}+p$ resonance states to $^{16}\mathrm{O}$ final states over the decay via γ emission to bound states in $^{20}\mathrm{Ne}$. Traditionally, the $^{19}\mathrm{F}(p,\alpha)^{16}\mathrm{O}$ reaction is estimated to be three to four orders of magnitude stronger compared to the $^{19}\mathrm{F}(p,\gamma)^{20}\mathrm{Ne}$ radiative capture reaction [23] (see Fig. 1).

The experimental confirmation of the predicted reaction rates for both reaction channels was troubled for the longest time by a lack or insufficiency of experimental data. Despite several efforts to measure the cross sections, remarkably little has been published. The reactions $^{19}\mathrm{F}(p,\alpha_0)^{16}\mathrm{O}$ and $^{19}\mathrm{F}(p,\alpha_{(2,3,4)})^{16}\mathrm{O}$ have been measured extensively in the low-energy range by Lorenz-Wirzba [24] between $E_p = 0.14$–0.90 MeV (with data published by Herndl *et al.* [25]) and by Ott [26] between $E_p = 0.20$–1.64 MeV, but the majority of these experimental results are not published in peer reviewed articles.

More recently, Dababneh *et al.* [27], Spyrou *et al.* [28], Spyrou *et al.* [29], and Couture *et al.* [30] have made additional measurements of the $^{19}\mathrm{F}(p,\alpha_{(2,3,4)})^{16}\mathrm{O}$ reactions, largely confirming previous results but significantly improving measurement precision. However, recent direct measurements by Lombardo *et al.* [31,32] and via the Trojan Horse method (THM) by LaCognata *et al.* [33,34] and Indelicato *et al.* [35], have observed an enhancement in the low-energy $^{19}\mathrm{F}(p,\alpha_0)^{16}\mathrm{O}$ cross section. Strikingly, there have been no modern measurements of the $^{19}\mathrm{F}(p,\alpha_1)^{16}\mathrm{O}$ reaction at low energies.

Experimental information is sparse about the competing $^{19}\mathrm{F}(p,\gamma)^{20}\mathrm{Ne}$ reaction which would trigger the breakout from the CNO cycles. The measurements are difficult because of the enormous background count rate from the $^{19}\mathrm{F}(p,\alpha_{(2,3,4)})^{16}\mathrm{O}$ reaction. The presently tabulated reaction rate is rather outdated and carries substantial uncertainties [20]. The rate is based primarily on a low-energy study of the $^{19}\mathrm{F}(p,\gamma)^{20}\mathrm{Ne}$ reaction by Subotić *et al.* [36] in the energy range between 0.30 and 1.20 MeV. However, it should be noted that significantly different resonance strengths were found in many cases between Subotić *et al.* [36] and the previous measurements by Farney *et al.* [37], Keszthelyi *et al.* [38], and Berkes *et al.* [39]. A recent measurement using the *Q*-value gating technique measured the dominant (p,γ_1) branch of the cross section between 200 and 760 keV [30]. While the low-energy resonance at $\mathrm{E_{c.m.}} = 213$ keV was not observed, an upper limit of $\omega\gamma = 60$ meV was established. The resonance strengths for the other resonances were generally smaller than those previously reported, and the net interference effect at low energies was seen to be destructive.

There is also very limited experimental information available regarding threshold states, subthreshold states, and direct capture strengths. Betts *et al.* [40] reported a 1^+ state near threshold via the $^{19}\mathrm{F}(^3\mathrm{He},d)^{20}\mathrm{Ne}$ reaction. Kious [41] then made a more targeted study, with the $^{19}\mathrm{F}(p,\alpha)^{16}\mathrm{O}$ reaction specifically in mind. They observed the same state found by Betts *et al.* [40], but a more precise determination of the energy was obtained. Detailed *R*-matrix calculations were also performed by Kious [41] to demonstrate possible interference

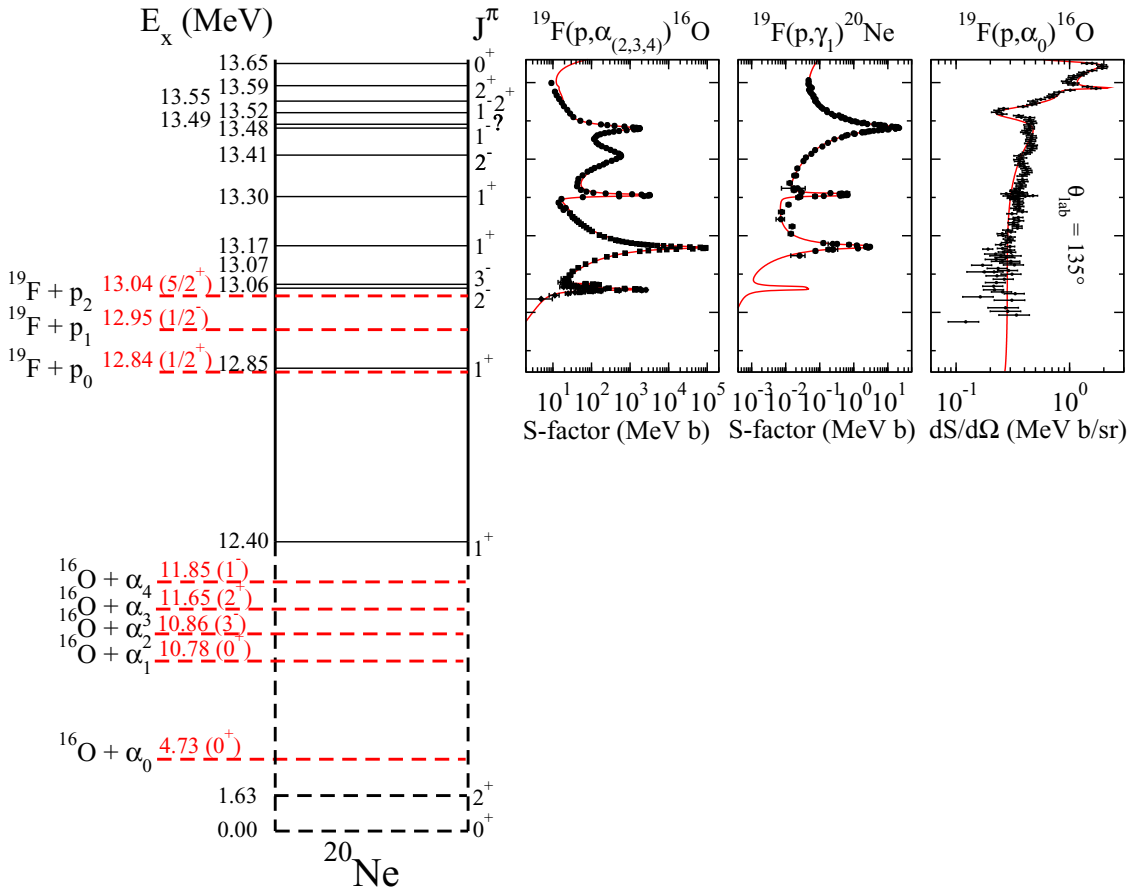

FIG. 1. Level diagram of the ^{20}Ne system, in the vicinity of the proton separation energy, showing the level properties relevant for the present R-matrix analysis of ^{19}F + p reactions. Separation energies are indicated by the red dashed horizontal lines, while levels in ^{20}Ne by black horizontal lines. Note that the lower part of the level diagram, below the real level at $E_x = 12.40$ MeV, is not to scale.

between the near threshold resonance (at $E_p = 11.5$ keV) and other higher lying resonances for the ^{19}F(p, α_2) ^{16}O reaction. No peer reviewed results have been published however.

This paper seeks to combine these past experimental results into a more cohesive multichannel R-matrix analysis [42] that includes all available ^{19}F + p data. This work begins with a review of the past literature that reports cross-section measurements for the ^{19}F + p reactions in Sec. II. The data are then subjected to an R-matrix analysis as described in Sec. III, and systematic uncertainties are found to dominate. Section IV comprises discussions on several features of the data and the analysis. Based on these considerations, a revised reaction rate with uncertainty estimates is presented in Sec. V. The implications for the Ca production in Pop III stars are discussed in Sec. VI while Sec. VII provides a summary.

II. REVIEW OF DATA FROM THE LITERATURE

For a comprehensive R-matrix analysis of the ^{19}F(p, α) ^{16}O and ^{19}F(p, γ) ^{20}Ne reactions, ideally, data for all reactions that populate the ^{20}Ne compound system over the excitation energy range of interest should be included. In this work, previous analyses are improved on by including the ^{19}F(p, $\alpha_{(0,1,2,3,4)}$) ^{16}O, ^{19}F(p, p_0) ^{19}F, and ^{19}F(p, γ_1) ^{20}Ne reactions in a simultaneous R-matrix analysis. Unfortunately no ^{19}F(p, $p_{(1,2)}$) ^{19}F or ^{19}F(p, γ) ^{20}Ne data to other final states are available. Measurements of these reactions are experimentally possible and are recommended to improve this type of global analysis in the future. Because of the complexity of several open channels and high-level density, the analysis has be limited to $E_p \lesssim 0.8$ MeV, which allows for an accurate calculation of the reaction rate up to ≈1 GK.

As noted in Sec. I, reactions proceeding through the $J^\pi = 0^+$ ^{16}O + $\alpha_{(0,1)}$ channels (see Fig. 1) are limited to natural parity states, while those going through the other channels can populate all states in the compound nucleus. This has the practical consequence that the ^{19}F(p, α_0) ^{16}O and ^{19}F(p, α_1) ^{16}O cross sections exhibit a nearly completely different set of resonances and underlying states then those populated in the ^{19}F(p, $\alpha_{(2,3,4)}$) ^{16}O and ^{19}F(p, $\gamma_{(0,1)}$) ^{20}Ne reactions. In addition, it is important to note that the first excited state to ground state decay in ^{16}O can not proceed via γ-ray emission ($0^+ \rightarrow 0^+$ transition) and instead decays primarily via pair-production. Therefore, only the ^{19}F(p, $\alpha_{(2,3,4)}$) ^{16}O reactions can be observed through secondary γ-ray emission. Note that the γ-ray decays of the excited states in ^{16}O do so with nearly 100% probability

directly to the ground state [43], simplifying secondary γ-ray measurements.

Its important to note some alternative notations that have been used in some previous literature. The most prolific is the notation $^{19}\mathrm{F}(p,\alpha\gamma)\,^{16}\mathrm{O}$, which refers to the $^{19}\mathrm{F}(p,\alpha_{(2,3,4)})\,^{16}\mathrm{O}$ reactions, emphasizing their detection via secondary γ-ray emission. A similar alternative notation, $^{19}\mathrm{F}(p,\alpha_\pi)\,^{16}\mathrm{O}$, is often used for the $^{19}\mathrm{F}(p,\alpha_1)\,^{16}\mathrm{O}$ reaction to emphasize its primary decay mode of pair production. It should also be noted that some early works refer to the $E_x = 6.13$ MeV transition as the $^{19}\mathrm{F}(p,\alpha_1)\,^{16}\mathrm{O}$ reaction (see, e.g., the level diagram in Berkes *et al.* [39]), as it is the first to decay via secondary γ-ray emission. Since this work primarily uses *R*-matrix to analyze each of the reactions individually, the notation using the individual number of the final state will be used for clarity.

The above nuclear properties rather naturally allow for the analysis of these different groups of reactions to be broken up into separate calculations. This was the strategy largely followed in past works, including the recent work of Lombardo *et al.* [44], where the focus was on the analysis of the $^{19}\mathrm{F}(p,\alpha_0)\,^{16}\mathrm{O}$ and $^{19}\mathrm{F}(p,\alpha_1)\,^{16}\mathrm{O}$ reactions over a much broader energy range than that investigated in this work.

A. $^{19}\mathrm{F}(p,\alpha_{(0,1)})\,^{16}\mathrm{O}$

Lombardo *et al.* [44] performed a comprehensive analysis of the $^{19}\mathrm{F}(p,\alpha_{(0,1)})\,^{20}\mathrm{Ne}$ reactions from near threshold up to $E_p \approx 10$ MeV and reviews of the relevant literature covering measurements up to those energies can be found there. As this work focuses on the low-energy range below $E_p < 0.8$ MeV, the data are limited to those of Refs. [24,25,31,35,45–49] for the $^{19}\mathrm{F}(p,\alpha_0)\,^{20}\mathrm{Ne}$ reaction and Refs. [49,50] for the $^{19}\mathrm{F}(p,\alpha_1)\,^{20}\mathrm{Ne}$ reaction. The data from Ott [26] are also examined but, because of large experimental effect corrections, the majority of the data are not included in the present analysis. Data for the $^{19}\mathrm{F}(p,\alpha_{(0,1)})\,^{20}\mathrm{Ne}$ reactions considered in the *R*-matrix fit are shown in Figs. 2–5.

As discussed recently in Lombardo *et al.* [44], there is rather significant inconsistency between the low-energy data of Lombardo *et al.* [32] and that of Lorenz-Wirzba [24] below $E_{\mathrm{c.m.}} \approx 0.5$ MeV. In this analysis, the data of Lorenz-Wirzba [24] are fit at low energy to purposely investigate another fit solution to better gauge the uncertainty in the low-energy *S* factor. This choice does not represent a preference of one data set over another. Additional measurements are needed to resolve this discrepancy.

B. $^{19}\mathrm{F}(p,\alpha_{(2,3,4)})\,^{16}\mathrm{O}$

One of the main focuses of this work is the analysis of the $^{19}\mathrm{F}(p,\alpha_{(2,3,4)})\,^{20}\mathrm{Ne}$ reaction channels, which were not investigated in Lombardo *et al.* [44]. As the corresponding excited states in $^{16}\mathrm{O}$ decay with nearly 100% probability to the ground state via γ-ray emission, these reactions are often studied through the detection of secondary γ rays. References [24,29,30,38,39,51,52] all include cross-section data for these reactions determined using γ-ray detection. The data of Devons *et al.* [51] and Spyrou *et al.* [29] report the sum over all three of these transitions. The only particle detection experiment is that reported in Ott [26], where a thin gas target was utilized. The other data sets from Ott [26] are compared with the fit, but are not included in it, due to the large experimental effects corrections needed for the thick TaF_5 targets that were employed. Data for the 6.13 MeV transition are shown in Figs. 6 and 9, the 6.92 MeV transition in Fig. 11, and the 7.12 MeV transition in Fig. 12. Figure 10 shows data for the sum of all three transitions and Figures 7 and 8 show secondary γ-ray angular distributions.

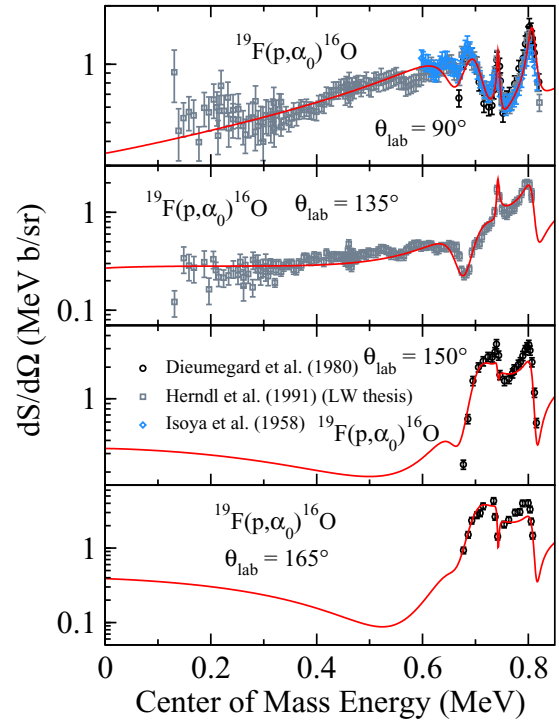

FIG. 2. Differential *S* factors of the $^{19}\mathrm{F}(p,a_0)\,^{16}\mathrm{O}$ data [24,25,45,48].

C. $^{19}\mathrm{F}(p,p_0)\,^{19}\mathrm{F}$

Following Lombardo *et al.* [44], the $^{19}\mathrm{F}(p,p_0)\,^{19}\mathrm{F}$ data of Caracciolo *et al.* [49] are included. The current analysis is expanded to also include the data of Webb *et al.* [53], where simulation of experimental effects were necessary. The data are shown in Fig. 13.

D. $^{19}\mathrm{F}(p,\gamma)\,^{20}\mathrm{Ne}$

Data for the $^{19}\mathrm{F}(p,\gamma)\,^{20}\mathrm{Ne}$ reaction are very limited. The only cross-section data are those of Couture *et al.* [30] and only for the $^{19}\mathrm{F}(p,\gamma_1)\,^{20}\mathrm{Ne}$ transition. Thick target yield studies of the narrow levels in this region report only small branchings to the ground state as summarized in Table 20.24 of the compilation [54]. The data of Couture *et al.* [30] are shown in Fig. 14.

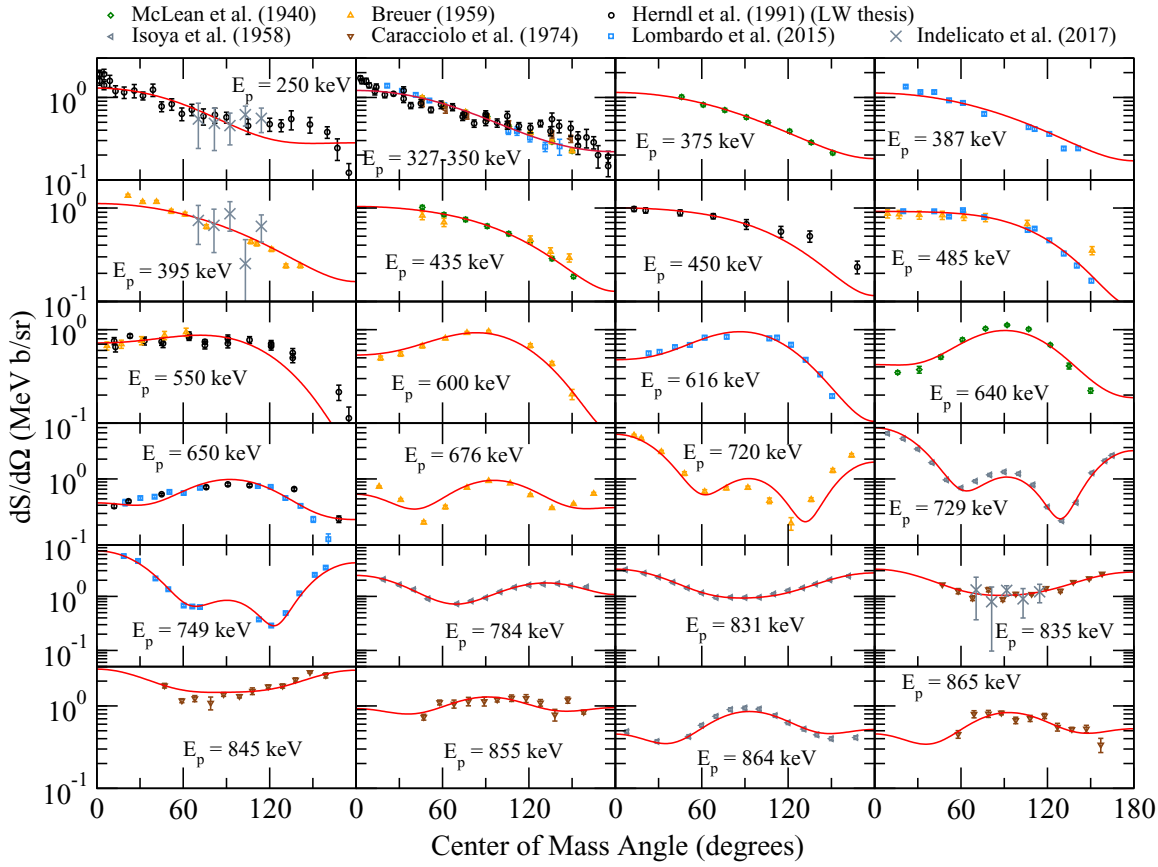

FIG. 3. Low-energy angular distributions for the ^{19}F(p, α_0) ^{16}O reaction [24,25,32,35,46–49].

E. Other reaction channels

Ideally, this work would also include a full analysis of the ^{16}O + α reactions over the overlapping excitation energy range. ^{16}O(α, α_0) ^{16}O cross sections over this excitation

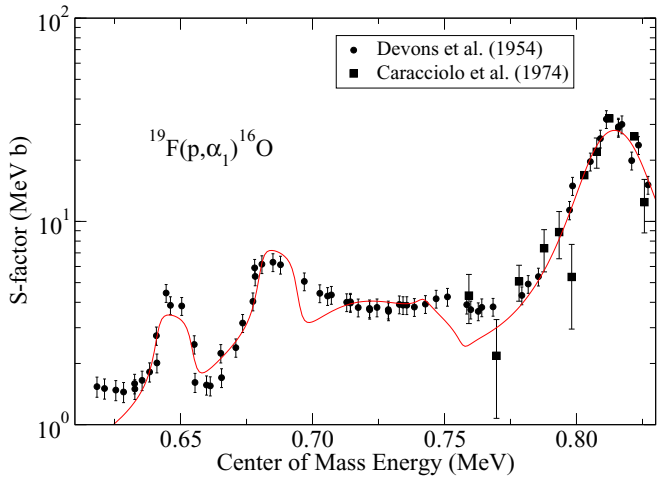

FIG. 4. Lowest-energy angle integrated ^{19}F(p, α_1) ^{16}O data of Devons *et al.* [50] and Caracciolo *et al.* [49]. The data of Devons *et al.* [50] has been renormalized as suggested in Lombardo *et al.* [44]. The R-matrix cross section (red line) has been convoluted with the energy resolution of the experiment.

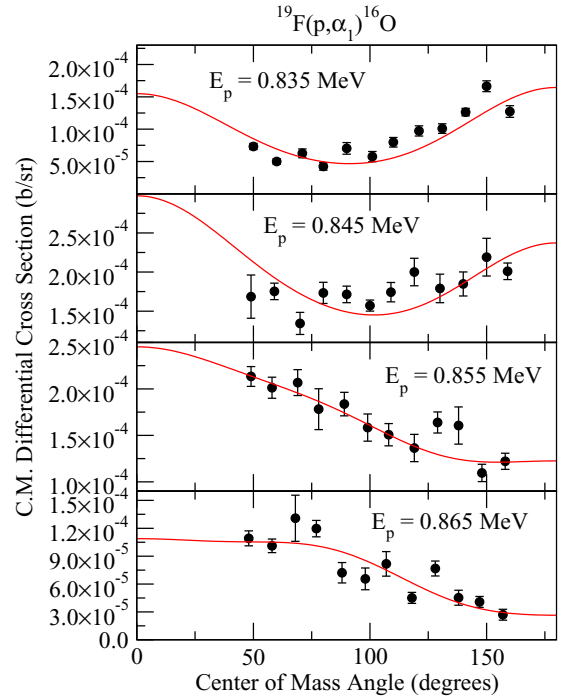

FIG. 5. Angular distributions of the ^{19}F(p, α_1) ^{16}O reaction from Caracciolo *et al.* [49].

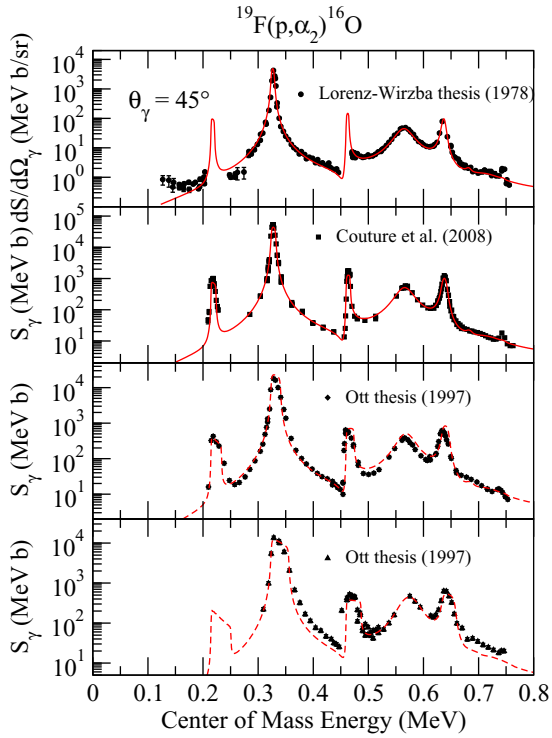

FIG. 6. The R-matrix fit to the ^{19}F$(p,\alpha_2)^{16}$O secondary γ-ray data of Lorenz-Wirzba [24] and Couture *et al.* [30] is shown by the red solid line. Additional data from Ott [26], which used substantially thicker targets, was not included in the fit, but calculations are shown (red dashed lines) comparing the R-matrix fit from this work convoluted with the experimental resolution.

energy range are reported by Caskey [55] and Mehta *et al.* [56]. However, because of the large difference in the α particle ($S_\alpha = 4.730$ MeV) and proton separation ($S_p = 12.844$ MeV) energies in ^{20}Ne, the excitation energy range for low-energy ^{19}F $+p$-induced reactions corresponds to a high energy range for ^{16}O $+\alpha$ induced reactions. It is thus possible to excite a large number of high spin states in the ^{16}O$(\alpha,\alpha_0)^{16}$O reaction, complicating the R-matrix analysis of these reactions.

Additionally, no previous R-matrix analyses of the ^{16}O $+\alpha$ reactions have extended up high enough in energy to exceed S_p. Currently, the low-energy range has been analyzed using R-matrix by Costantini *et al.* [57], focusing on the ^{16}O$(\alpha,\gamma)^{20}$Ne reaction. At higher energies, Berthoumieux *et al.* [58] analyzed ^{16}O$(\alpha,\alpha)^{16}$O data from $E_\alpha = 3.0$ to 3.4 MeV and more recently Nauruzbayev *et al.* [59] and Hao *et al.* [60] have performed fits to limited sets of data up to $E_\alpha = 6.25$ MeV and $E_\alpha = 9.0$ MeV respectively. However, these higher energy analyses were limited to backward angle data and still do not exceed the proton threshold which corresponds to $E_\alpha = 10.14$ MeV.

As discussed in Lombardo *et al.* [44], of particular interest are the ^{16}O$(\alpha,\alpha_1)^{16}$O data of Laymon *et al.* [61]. In that work, a strong 2^+ resonance was identified at $E_\alpha = 10.45$ MeV ($E_x = 13.09$ MeV), which would correspond to $E_p \approx 260$ keV for the ^{19}F$(p,\alpha_1)^{16}$O reaction. The general trend of the data can be reproduced with a broad 2^+ state, but it is clear that the angular distribution is distorted from that of an isolated resonance, indicating contributions from other weaker nearby levels. This is shown by the partial wave analysis in Fig. 4 of Laymon *et al.* [61]. Additional measurements are highly desirable for this reaction.

A significant amount of data is also available for the β-delayed α decay spectrum of ^{20}Na$(\beta\alpha)^{16}$O [62,63]. The decay has been observed to proceed strongly through several 2^+ states via allowed transitions. While the cutoff energy is at $E_x = 13.89$ MeV, extending above the proton separation energy in ^{20}Ne, even the high statistics measurement of Laursen *et al.* [62] only observes decays up to $E_x \approx 11.9$ MeV. Therefore, while these data could prove quite useful in a global fitting at lower energies, levels in the present region of interest have not yet been observed.

F. Transfer reactions

While transfer reaction data is not included directly in the R-matrix analysis, the level information for near threshold levels is of vital importance in the extrapolation of the cross section to the astrophysically relevant energy region. In this case, a strong 1^+ near-threshold level has been identified using the ^{19}F$(^3$He, d$)^{20}$Ne reaction by Betts *et al.* [40] and Kious [41] at $E_{\text{c.m.}} = 11$ keV. This resonance has the potential to strongly affect both the ^{19}F$(p,\alpha_{(2,3,4)})^{16}$O and ^{19}F$(p,\gamma)^{20}$Ne reactions. In addition, Kious [41] reports a subthreshold level at $E_{\text{c.m.}} = -448$ keV. A dedicated study seems past due to determine the proton ANCs of the bound state levels in ^{20}Ne to evaluate possible subthreshold resonance contributions and interference in the low-energy cross section.

III. *R*-MATRIX ANALYSIS

Based on the discussions presented in Sec. II, the present R-matrix analysis includes the reactions ^{19}F$(p,\alpha_{(0,1,2,3,4)})^{16}$O, ^{19}F$(p,p_0)^{19}$F, and ^{19}F$(p,\gamma_1)^{20}$Ne. There are no cross-section data available to constrain the branchings to the ^{19}F$(p,p_{(1,2)})^{19}$F, ^{19}F$(p,\gamma_0)^{20}$Ne, or other higher lying γ-ray decay channels. Tilley *et al.* [54] and Lombardo *et al.* [44] do report some significant branchings to the ^{19}F$(p,p_{(1,2)})^{19}$F channels for the highest lying resonance considered in this analysis (see Table II), therefore the p_1 channel is included for this resonance and a background state. It should also be noted that the present analysis stops just below the multi-particle breakup threshold, ^{12}C $+2\alpha$, at $E_x = 13.79$ MeV.

For the R-matrix fits, the code AZURE2 [64,65] has been used. As is standard for the code, the alternative R-matrix formalism of Brune [66] is used to work directly with physical widths and resonance energies. In addition, a modified version of the code was created that included the formalism for secondary γ-ray angular distributions as reported in Brune and deBoer [67] and the ability to sum the cross sections for multiple reactions (for the ^{19}F$(p,\alpha_{(2,3,4)}\gamma)^{20}$Ne reaction data of Devons *et al.* [51] and Spyrou *et al.* [29]). The masses, separation energies, and channel radii used for the R-matrix fit are given in Table I. The fit to the data is shown in Figs. 2–14 and the best fit parameters are given in Table II.

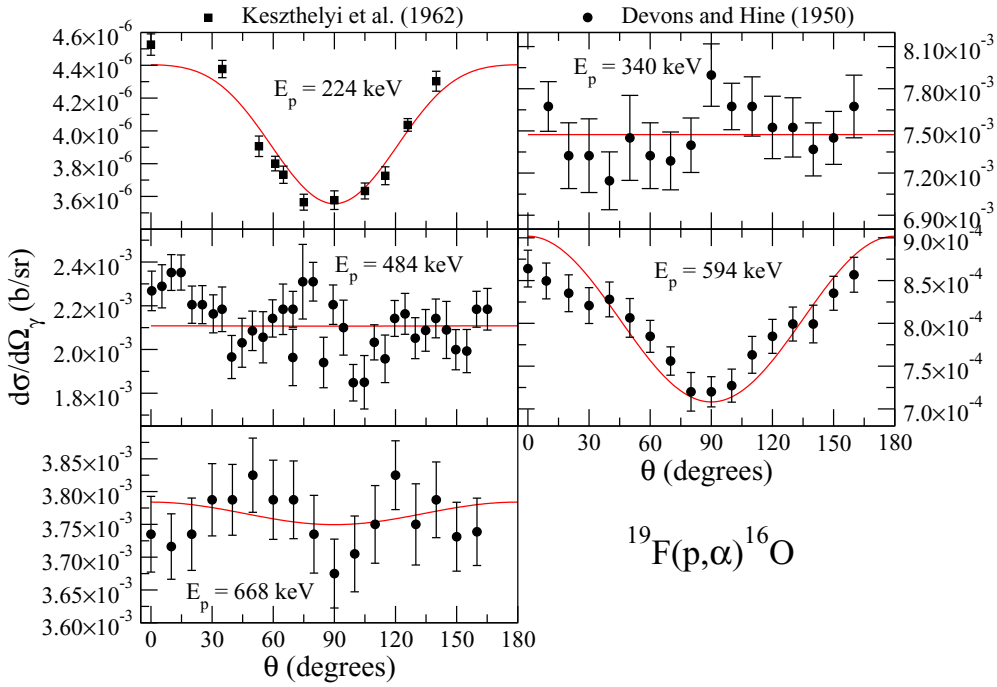

FIG. 7. Secondary on-resonance γ-ray angular distribution measurements for the ^{19}F(p, $\alpha_{(2,3,4)}$) ^{16}O reactions [38,51]. The data of Devons *et al.* [51] are the sum of the three secondary γ-ray transitions while that of Keszthelyi *et al.* [38] are of only the ^{19}F(p, α_2) ^{16}O reaction.

In general, the R-matrix fit was able to reproduce the ^{19}F $+p$ data described in Sec. II. For the ^{19}F(p, α_0) ^{16}O data, both the energy and angular dependence of the low-energy cross section was well described as demonstrated in Figs. 2 and 3. The lowest-energy region, below $E_{\text{c.m.}} = 0.65$ MeV, is smoothly varying in energy and the data could be described using only broad background resonances of $J^\pi = 0^+$ and 1^-. In fact, it was possible to eliminate all of the higher-energy levels used in the high energy fit of Lombardo *et al.* [44], above $E_x = 13.7$ MeV, and replace their contributions with one or two background states (see Table II), for each J^π, to simplify the fitting procedure of the low-energy region. The narrow resonances that are observed in the ^{19}F(p, α_0) ^{16}O data, above $E_{\text{c.m.}} = 0.65$ MeV, were reproduced in a similar manner as Lombardo *et al.* [32]. It is observed that the angular distribution data of Lorenz-Wirzba [24] seem to be systematically above other measurements at backward angles. There are weak fluctuations at low energy in the ^{19}F(p, α_0) ^{16}O data that may be the result of additional weak resonance contributions, but they are of a similar magnitude as the error bars of the

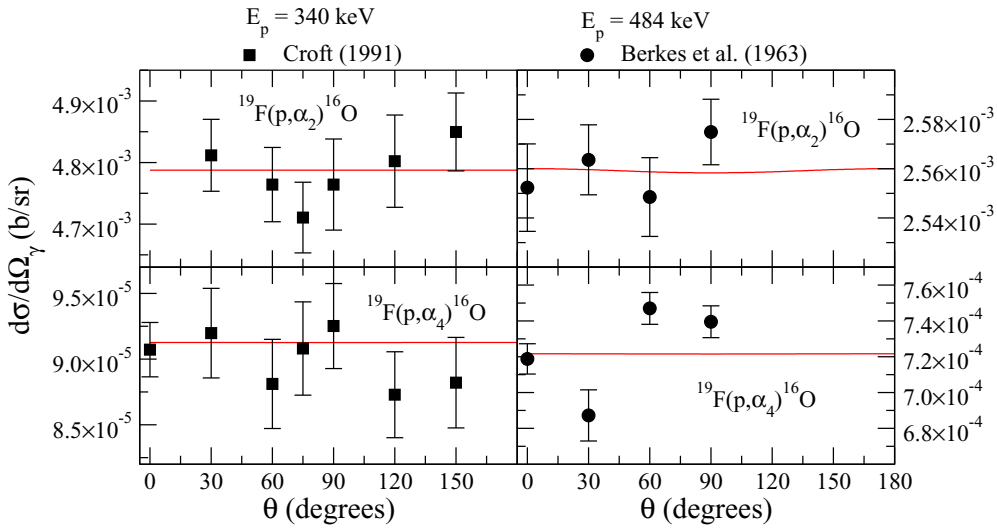

FIG. 8. Secondary on-resonance γ-ray angular distribution measurements for the ^{19}F(p, $\alpha_{(2,4)}$) ^{16}O reactions at $E_p = 340$ keV [52] and 484 keV [39]. The isotropic distributions of these isolated resonances provide accurate relative angular distribution calibrations for γ-ray detectors.

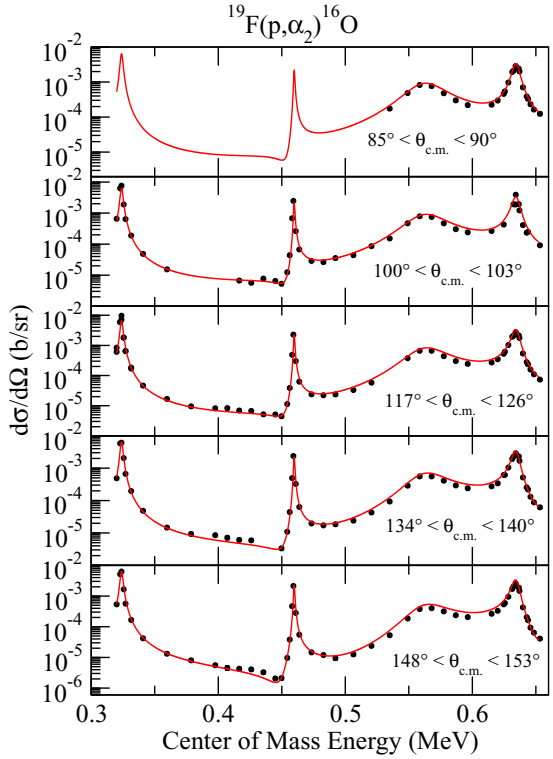

FIG. 9. Differential cross-section measurement of the $^{19}\mathrm{F}(p,\alpha_2)^{16}\mathrm{O}$ reaction though observation of the α-particles. This thin target data set from Ott [26] is unique for this reaction, as all others have been made by measuring secondary γ rays.

experimental data in that region. As discussed in Sec. II A, the data of Ref. [32] are not included in the fit, as well as the two very low-energy resonances reported in the THM study of LaCognata *et al.* [33], as they were not needed to reproduce the data that were considered. Further discussions can be found in Sec. IV A.

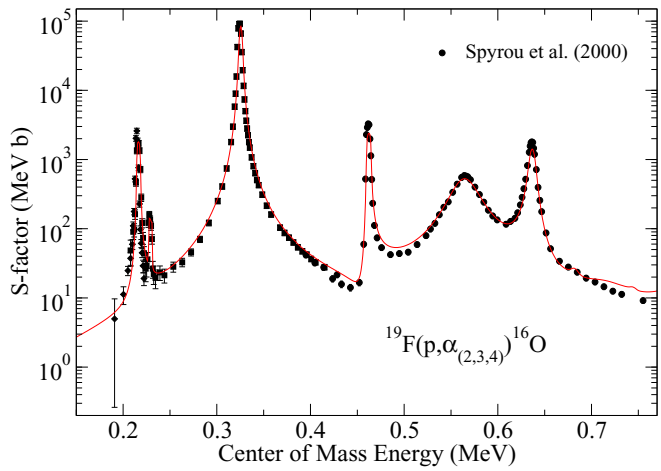

FIG. 10. Sum of the $^{19}\mathrm{F}(p,\alpha_{(2,3,4)})^{16}\mathrm{O}$ reactions measured with a sodium iodide summing detector by Spyrou *et al.* [29]. The *R*-matrix cross section (red line) has been convoluted with the energy resolution of the experiment.

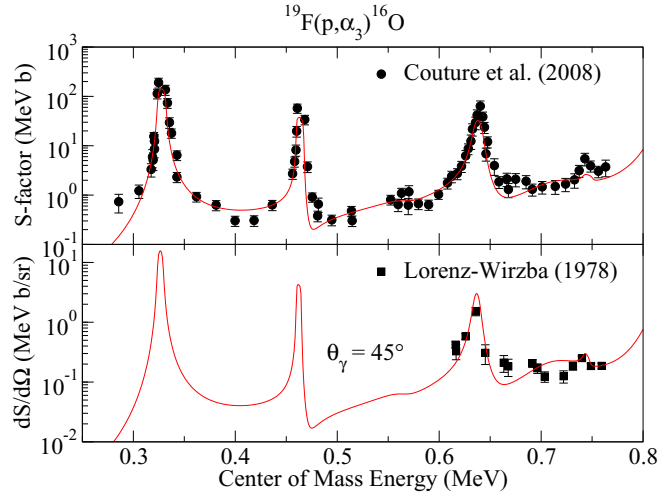

FIG. 11. Experimental data for the $^{19}\mathrm{F}(p,\alpha_3)^{16}\mathrm{O}$ reaction. The top panel displays the angle integrated data of Couture *et al.* [30] (circles) while the bottom panel shows the differential data of Lorenz-Wirzba [24] (squares) at $\theta_\gamma = 45°$. The *R*-matrix cross section (red line) has been convoluted with the energy resolution of the experiment.

The limited amount of low-energy $^{19}\mathrm{F}(p,\alpha_1)^{16}\mathrm{O}$ data [49,50] could be described by the same resonances observed over this energy region in the $^{19}\mathrm{F}(p,\alpha_0)^{16}\mathrm{O}$ data (see Figs. 4 and 5), although there are discrepancies between the data and fit in some off-resonance interference regions. The exception is the lowest-energy resonance at $E_{\mathrm{c.m.}} = 0.63$ MeV ($E_x = 13.48$ MeV) observed in the data of Devons *et al.* [50]. It is possible that this resonance corresponds to the 1^- level that is reported in the literature at $E_x = 13.48$ MeV ($\Gamma = 24(8)$ keV), but the resonance appears to be narrower, with a width of

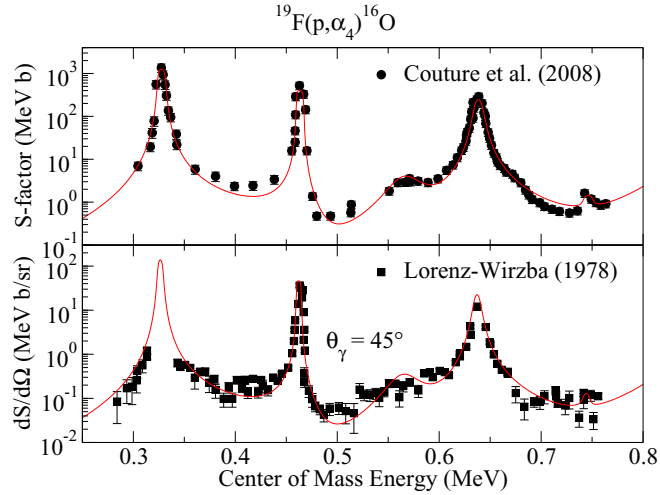

FIG. 12. Experimental data for the $^{19}\mathrm{F}(p,\alpha_4\gamma)^{16}\mathrm{O}$ reaction. The top panel displays the angle integrated data of Couture *et al.* [30] (circles) while the bottom panel shows the differential data of Lorenz-Wirzba [24] (squares) at $\theta_\gamma = 45°$. The *R*-matrix cross section (red line) has been convoluted with the energy resolution of the experiment.

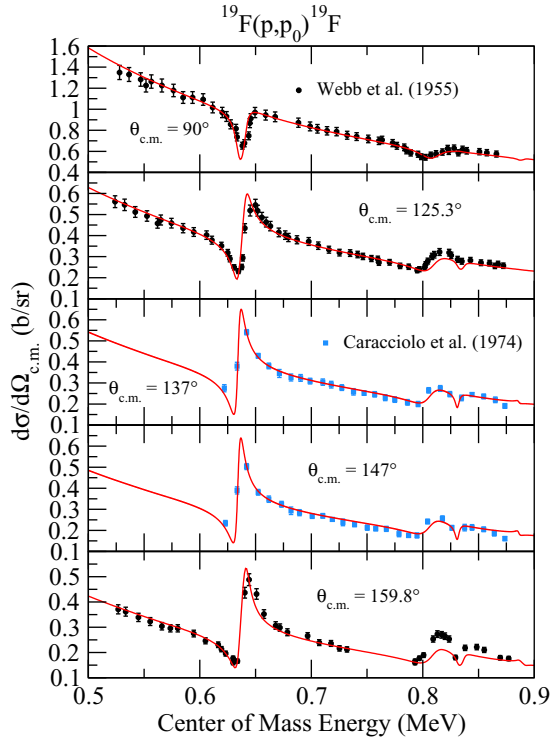

FIG. 13. The limited amount of proton scattering data from Webb *et al.* [53] and Caracciolo *et al.* [49]. The *R*-matrix cross section (red line) has been convoluted with the energy resolution of the experiment.

<10 keV. Since no angular distribution information is available in this low-energy region, this resonance has been fit using an arbitrary J^π assignment.

Almost none of the natural parity states that contribute strongly to the ^{19}F(p, $\alpha_{(0,1)}$) ^{16}O reactions contribute strongly to the ^{19}F(p, $\alpha_{(2,3,4)}$) ^{16}O reactions or the ^{19}F(p, γ_1) ^{20}Ne reaction, which are instead dominated by a shared set of resonances that correspond to unnatural parity states in the ^{20}Ne system. In particular, the cross section is dominated by contributions from only $J^\pi = 1^+$ and 2^- levels. The exceptions are the 2^+ level that is observed as a weak resonance at $E_x = 13.585$ MeV in all the ^{19}F(p, $\alpha_{(0,1,2,3,4)}$) ^{16}O reactions and the ^{19}F(p, p_0) ^{19}F reaction, and the 3^- level that is observed only in the ^{19}F(p, $\alpha_{(2,3,4)}$) ^{16}O sum data of Spyrou *et al.* [29] (see Table II).

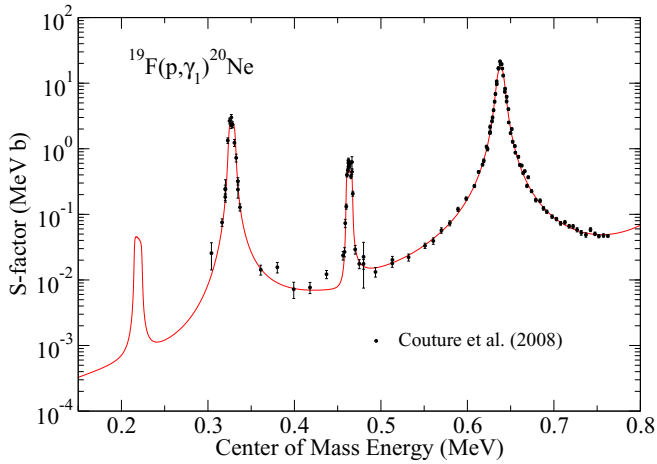

FIG. 14. Only the ^{19}F(p, γ_1) ^{20}Ne data of Couture *et al.* [30] are available for the capture reaction. The *R*-matrix cross section (red line) has been convoluted with the energy resolution of the experiment.

TABLE I. Atomic masses (M), particle separation (S), and channel radii (a) used in the *R*-matrix calculation. Atomic masses are in atomic mass units, separation energies in MeV, and channel radii in fm. Atomic masses and separation energies are taken from Audi *et al.* [68].

Parameter	Value
S_p	12.844 MeV
S_α	4.73 MeV
S_{α_1}	10.779 MeV
S_{α_2}	10.86 MeV
S_{α_3}	11.65 MeV
S_{α_4}	11.85 MeV
M_p	1.0078 u
M_α	4.0026 u
$M(^{16}\mathrm{O})$	15.9949 u
$M(^{19}\mathrm{F})$	18.9984 u
$M(^{20}\mathrm{Ne})$	19.9924 u
$a_{p_{(0,1,2)}}$	5.136 fm
$a_{\alpha_{(0,1,2,3,4)}}$	5.75 fm

Two sets of experimental data dominate the fit for the ^{19}F(p, $\alpha_{(2,3,4)}\gamma$) ^{16}O reactions (see Figs. 6 and 10), the partial cross sections of Couture *et al.* [30] and the γ-ray sum data of Spyrou *et al.* [29]. While Couture *et al.* [30] used a multilevel Breit-Wigner analysis to fit their cross-section data, it was found that their parameters resulted in a very good starting point for the *R*-matrix fit for this reaction.

The data of Spyrou *et al.* [29] were found to be generally consistent with other data sets, especially the higher-energy portion of their data. The two other lower-energy data sets required a shift of ≈6 keV up in energy, even after corrections for target energy loss. However, the shifted data then also agree with the resonance energies quoted in Table 1 of that work. The low-energy Spyrou *et al.* [29] data were made with a thin target at these low energies, allowing for the resolution of a new narrow resonance at $E_{\mathrm{c.m.}} = 225$ keV, which corresponds to a 3^- level at $E_x = 13.07$ MeV that is just above the previously measured stronger resonance at $E_{\mathrm{c.m.}} = 214$ keV corresponding to the 2^- state at $E_x = 13.06$ MeV.

In addition, the thesis data of Lorenz-Wirzba [24], which were published in Ref. [25], were also included in the fit. The secondary γ-ray angular distribution formalism of Brune and deBoer [67] was used to fit these differential cross-section measurements at $\theta_{\mathrm{lab}} = 45^\circ$. The data include very low-energy, thin-target, differential cross-section measurements for the ^{19}F(p, $\alpha_{(2,4)}$) ^{16}O reactions (see Figs. 6 and 12). While the *R*-matrix fit was able to accurately reproduce the ^{19}F(p, α_2) ^{16}O differential cross-section data of Lorenz-Wirzba [24] over the majority of the energy range, larger discrepancies do

TABLE II. *R*-matrix parameters from the best fit to the ^{19}F+p data considered in this work. Levels marked as "BG" are background levels, and do not correspond to individual levels in the compound system. When two values are given for a partial width, they correspond to either Γ_s/Γ_{s+1} or $\Gamma_\ell/\Gamma_{\ell+1}$, where s and ℓ correspond to the lowest channel spin or orbital angular momentum, respectively.

(keV)	(MeV)		(eV)							
$E_{\text{c.m.}}$	E_x	J^π	Γ_{p_0}	Γ_{p_1}	Γ_{α_0}	Γ_{α_1}	Γ_{α_2}	Γ_{α_3}	Γ_{α_4}	Γ_{γ_1}
214.9	13.0589	2^-	0.012				1.1×10^3	6.3	1.4	0.06[a]
227.9	13.0719	3^-	8.6×10^{-4}				87			
323.9	13.1679	1^+	35.8[a]				2.2×10^3	−7.0	62	−0.12
459.9	13.3039	1^+	12.1[a]				610	18	−200	0.21
562.7	13.4067	2^-	54				34×10^3	−1.9	−240	-1.0×10^{-3}
634.6	13.4786	1^+	6.5×10^3				−88	2.7	21	1.5
639.9	13.4836	1^-	0.14/−6.8		-87×10^3	-12×10^3	12×10^3			
641.2	13.4852	[b]	0.66		4.4×10^3					
681.0	13.5250	1^-	0.88		420	3.6×10^3	150			
709.0	13.5530	2^+	−16/−0.41		39×10^3	-8.9×10^3	-16×10^3	2.9×10^3		
742.4	13.5864	2^+	0.032/0.50		5.2×10^3	−8.4	18		195	
806.5	13.6505	0^+	13×10^3	7.6×10^3	−66	110	0.58			
	13.6752 (BG)	2^-	390/390	780				2.98×10^3		
	13.7300 (BG)	1^+	5.7×10^3/7.0×10^3				12	870	780	−1.7/−3.8
	13.8877 (BG)[c]	1^-	590/−590		730×10^3					
	13.9118 (BG)[c]	0^+	-1.4×10^3		390×10^3					
	14.0000 (BG)[c]	2^-	120×10^3					-7.5×10^3		
	20.9409 (BG)[c]	1^-	1.3×10^8/7.8×10^6		8.5×10^6	1.7×10^6				

[a]Fixed to the value given in Couture *et al.* [30].
[b]Spin-parity undetermined.
[c]Fixed.

occur around the low-energy resonance at $E_p = 225$ keV. The increase observed in the low-energy cross-section data may indicate additional structure at these low energies (see Sec. IV B).

There are also measurements of the ^{19}F$(p, \alpha_{(2,3,4)})^{16}$O and ^{19}F$(p, \gamma_1)^{20}$Ne reactions given in the unpublished thesis of Ott [26]. The majority of these data sets use thick TaF_5 targets repeating energy ranges already covered by thinner target measurements. The exception to this are the thin gas target differential cross-section measurements of the ^{19}F$(p, \alpha_2)^{16}$O reaction made through direct α-particle detection. These data are included in the fit and are found to be in good agreement with the other thin target data sets. See further discussion in Sec. IV D.

There are only two sets of low-energy ^{19}F$(p, p_0)^{19}$F data available in the literature [49,53] and unfortunately no ^{19}F$(p, p_{(1,2)})^{19}$F measurements. The spin assignments of Lombardo *et al.* [44] are adopted and a reasonably consistent fit is obtained. The data of Webb *et al.* [53] required corrections for target resolution and energy loss, which is why they were not used previously in the analysis of Lombardo *et al.* [44].

The experimental ^{19}F$(p, \gamma)^{20}$Ne data of Couture *et al.* [30] are described well by the levels reported in the literature [54], and are the same as those populated in the ^{19}F$(p, \alpha_{(2,3,4)})^{16}$O reactions. As in Couture *et al.* [30], a background 1^+ level was needed to modify the off-resonance interference shape produced by only the levels in the experimentally observed region. Since the data could be reproduced without lower-energy resonance or direct capture contributions, these components were not included in the fit. However, their effects on the extrapolation of the cross section to lower energies are discussed in Sec. IV G. The *R*-matrix fit to the capture data of Couture *et al.* [30] is shown in Fig. 14.

IV. DISCUSSION

A. Inconsistencies between different ^{19}F$(p, a_0)^{16}$O and THM measurements

While most of the ^{19}F$(p, a_0)^{20}$Ne data from the literature are in good general agreement [69], a significant discrepancy has been observed between the data of Lorenz-Wirzba [24] and Lombardo *et al.* [32]. The data are in reasonable agreement at higher energies above $E_{\text{c.m.}} \approx 0.5$ MeV but increasingly diverge at lower energies, where the data of Lombardo *et al.* [32] are significantly higher in cross section than that of Lorenz-Wirzba [24]. Additionally, the THM measurements of LaCognata *et al.* [33] report two resonances at low energy, which should just overlap the lowest-energy data of Lorenz-Wirzba [24]. However, the widths given by LaCognata *et al.* [33] produce a cross section that does not appear to be consistent with the experimental data of Lorenz-Wirzba [24]. Therefore, the main low-energy uncertainty in the ^{19}F$(p, a_0)^{20}$Ne S-factor results from the systematic differences in these data sets. The data of Lorenz-Wirzba [24] set a lower limit, while the data of LaCognata *et al.* [33] and Lombardo *et al.* [32] give an upper limit as shown in Fig. 15. These discrepancies are considered when determining

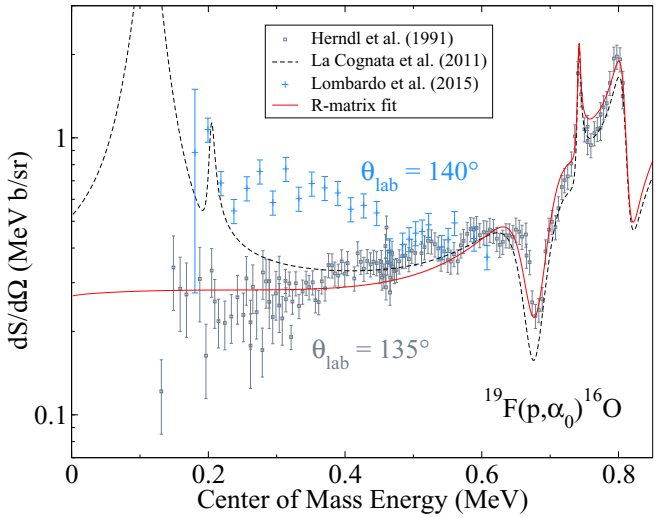

FIG. 15. Illustration of the inconsistencies between the low-energy data of Lorenz-Wirzba [24], the data of Lombardo *et al.* [32], and the THM measurements of LaCognata *et al.* [33].

the uncertainty in the reaction rate as discussed further in Sec. V.

B. The 11 keV threshold resonance

Transfer measurements using the ^{19}F(^{3}He, d) ^{20}Ne reaction data [40,41] have observed a near threshold level at E_p = 11.5 keV (E_x = 12.855 MeV) [41]. As the level is a 1^+ state, it can only contribute to the ^{19}F(p, $\alpha_{(2,3,4)}$) ^{16}O and ^{19}F(p, γ) ^{20}Ne reactions, although it will likely only make a significant contribution to the total cross section if its total width is dominated by Γ_{α_2}. The resonance is low enough in energy that it may not contribute to the rate at temperatures of interest, unless its total width is large enough to create significant interference with other higher lying resonances. The total width is highly uncertain [29,41], both Kious [41] and Spyrou *et al.* [29] have estimated upper limits for the total width based on the proton width determined from the transfer reaction and the resonance's interference with the higher-energy off-resonance cross-section data. Spyrou *et al.* [29] have estimated an upper limit of 120 eV using a Breit-Wigner analysis, but the present analysis, using a full multilevel R-matrix analysis, found that larger values are possible. The R-matrix analysis reveals that this upper limit is difficult to constrain because the off-resonance cross section over the region of the data could have additional contributions from higher lying resonances and/or subthreshold resonances. The upper limit from the experimental resolution of the transfer measurements is $\approx$ 1 keV [41], which is consistent with the upper limit estimate from the present R-matrix analysis. In addition, the ^{19}F(p, α_2) ^{16}O data of Lorenz-Wirzba [24] extend to even lower energies than that of Spyrou *et al.* [29] and give a larger cross section than is expected from the R-matrix fit to the higher-energy data, even with interference with the near threshold resonance. This may be an indication of other low-energy contributions to the cross section.

As shown in Fig. 16, if the near threshold state does have a Γ_{α_2} of $\approx$ 1 keV it can result in a low-energy cross section that is comparable to that of the ^{19}F(p, α_0) ^{16}O cross section, which has been assumed previously to dominate over these low energies [20]. This will also be considered as another source of uncertainty in the reaction rate estimate of Sec. V, as it has a significant effect on the upper limit.

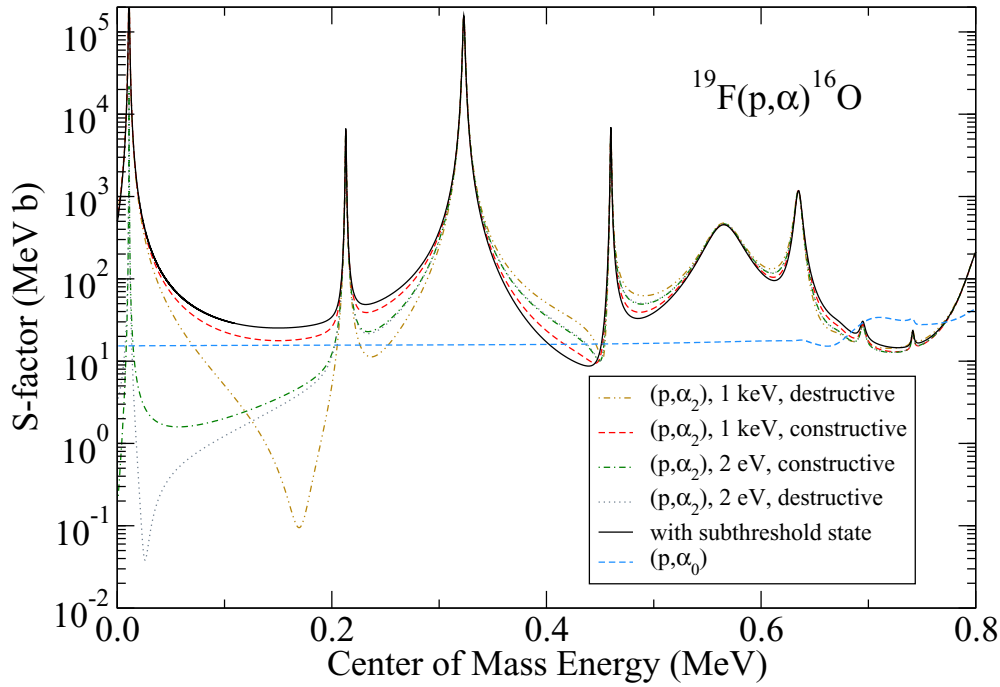

FIG. 16. Calculations of the ^{19}F(p, α_2) ^{16}O S factor given different interference scenarios and partial width limits for the near-threshold state at 11 keV. These should be compared with the blue dashed line, which corresponds to the nearly constant ^{19}F(p, α_0) ^{16}O S factor.

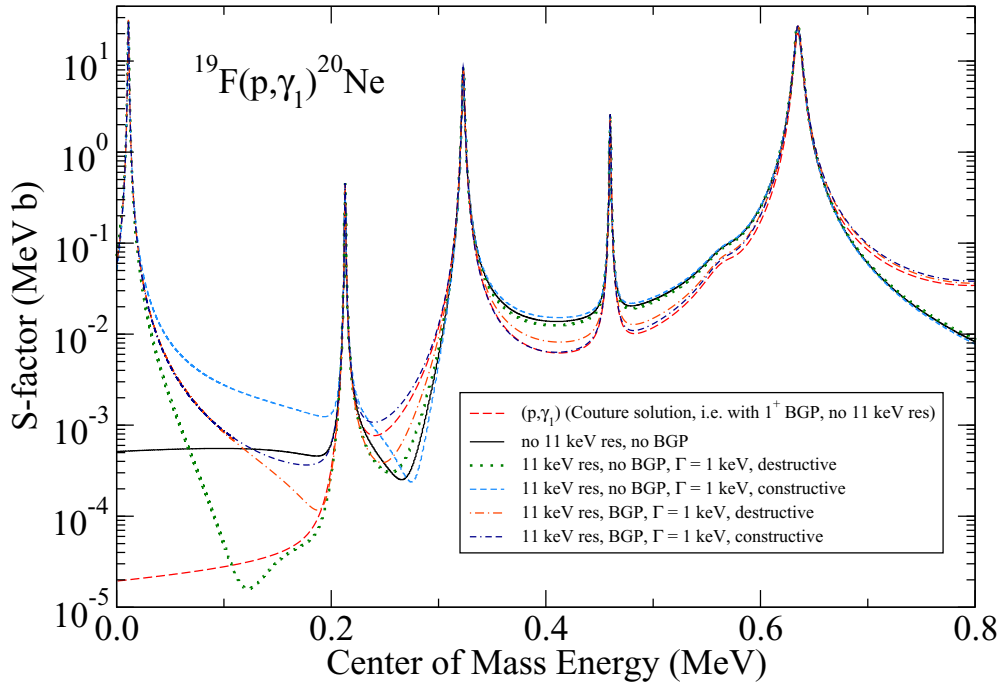

FIG. 17. Calculations of different interference scenarios given the width limitations of the near-threshold state at 11 keV.

While it has not been investigated in previous work, given the branching ratios of other nearby states, it is likely that the near-threshold state also has a significant decay branch through γ-ray emission to the first excited state of ^{20}Ne. Figure 17 shows example interference solutions for the upper limit width estimate ($\Gamma_{\alpha_2} = 1$ keV) of the near threshold state. As will be discussed further in Sec. V, the interference solutions have a significant effect on the (p, γ) reaction rate, due to their large modifications to the low-energy cross section.

C. 3$^-$ state observed in Spyrou *et al.* [29]

Spyrou *et al.* [29] observed a narrow low-energy resonance at $E_p = 237$ keV on the high energy side of the lowest-energy resonance observed at $E_p = 225$ keV in their sum data (see Fig. 10). Due to the close proximity of the two resonances, the only other experiment with similar resolution is that of Lorenz-Wirzba [24]. In that measurement, only data for the ^{19}F$(p, \alpha_2)\,^{16}$O cross section extends low enough in energy to possibly observe the resonance, but the data in this region do not have the sensitivity in yield.

D. Unpublished thesis results

There is a large body of experimental measurements available from experiments at the Universität Stuttgart, which are collected in the thesis of Ott [26]. The majority of these measurements use TaF_5 targets, which are significantly thicker than other measurements. Even when the *R*-matrix cross section is corrected for target resolution, these measurements deviate somewhat from thin target measurements. This may be the result of the approximations used to convert these data to angle integrated cross sections [26], or it could be the result of an insufficiently accurate convolution function given the large corrections necessary. For these reasons, these data were not included directly in the fitting. A comparison of the *R*-matrix fit with these data, approximately convoluted with the experimental target thickness, is shown in Fig. 6.

The exception to this are the thin target data taken with a gas target system where the differential cross section of the $p(^{19}\mathrm{F}, \alpha_2)\,^{16}$O reaction was determined in inverse kinematics through α-particle detection. This is a unique set of data as nearly all measurements of the ^{19}F$(p, \alpha_2)\,^{16}$O cross section have been made instead by observation of the secondary γ rays. Further, the excellent agreement of the *R*-matrix fit with the differential data, as shown in Fig. 9, gives added confidence in the spin-parity assignments of the levels that are populated in this reaction.

The transfer reaction measurements presented in the thesis of Kious [41] provide much of the information available for the near and subthreshold levels that likely play an important role in the low-energy cross section of the ^{19}F$(p, \alpha_{(2,3,4)})\,^{16}$O and ^{19}F$(p, \gamma)\,^{20}$Ne reactions. This has already been highlighted for the ^{19}F$(p, \alpha_{(2,3,4)})\,^{16}$O in Spyrou *et al.* [29]. The importance of the near threshold state, possible subthreshold contributions, and the limited previous measurements, provide solid motivations for new transfer studies.

Finally, the data presented in Lorenz-Wirzba [24] are published in Herndl *et al.* [25], but this work largely concentrates on comparisons of the data with zero-range distorted-wave Born approximation calculations and does not go into any details regarding the measurement of the experimental data.

E. Absolute normalization

The absolute normalization of the ^{19}F$(p, \alpha)\,^{16}$O cross section has proven to be challenging as is evidenced by the

TABLE III. Comparison of resonance strength measurements for narrow resonances in the ^{19}F(p, γ) ^{20}Ne reaction. The uncertainty in the strengths are taken as the systematic uncertainty in the cross-section measurement of Couture *et al.* [30] (16%). Table adopted from Angulo *et al.* [20].

$E_{r,\mathrm{c.m.}}$ (MeV)	E_x (MeV)	J^π	$\omega\gamma$ (eV)						Γ_{p_0} (eV)	Γ_{γ_1} (eV)	Γ_{total} (eV)
			[71]	[37]	[38]	[39]	[36]	this work	this work		
0.2148(10)	13.0588	2^-			$1.3(13)\times10^{-6}$			$<8.3\times10^{-7}$	0.012	<0.06[a]	1085
0.3239(10)	13.1679	1^+			$3.5(7)\times10^{-3}$		$10(2)\times10^{-3}$	$1.4(3)\times10^{-3}$	35.8[b]	0.12	2250
0.4599(10)	13.3039	1^+				$5(1)\times10^{-3}$	$1.6(4)\times10^{-3}$	$2.3(4)\times10^{-3}$	12.1[b]	0.21	834
0.5627(10)	13.4067	2^-				$20(2)\times10^{-3}$	$5.6(8)\times10^{-3}$	$<3.9\times10^{-3}$	53.6	< 2	34 600
0.6345(10)	13.4785	1^+	1.58(36)	1.58(36)			1.61(24)	1.1(2)	6480	1.5	6590

[a]Fixed at the upper limit of Couture *et al.* [30].
[b]Fixed at the value reported in Couture *et al.* [30].

discrepancies in absolute cross sections reported in different works, which deviate from each other by significantly more than their stated uncertainties. One likely reason is that fluorine targets often experience significant degradation after only a fraction of a Coulomb of beam bombardment with moderate beam intensities (10's of μA). Easily made, evaporated LiF targets are too unstable for the large beam intensities required for low-energy measurements, so CaF_2 or TaF_5 targets have been utilized instead. Even with these more stable targets, large discrepancies have been reported.

For the absolute normalization of the ^{19}F(p, $\alpha_{(2,3,4)}$) ^{16}O measurements, all other data have been normalized to those of Couture *et al.* [30], which were in turn found to be consistent with the strength measurement of Becker *et al.* [70] for the E_p = 324 keV resonance (see Sec. IV F. For the ^{19}F(p, $\alpha_{0,1}$) ^{16}O data, the normalization of Lombardo *et al.* [44] has been adopted. This particular normalization was adopted because the experiments of Becker *et al.* [70] were specifically focused on measuring absolute normalizations. This is reflected in the small uncertainty reported in their measurement of the E_p = 340 keV resonances strength (see Table IV).

F. Comparisons with strength measurements

This work improves on the narrow resonances formalism used by past works as the rate is obtained by numerical integration of the R-matrix cross section. This method allows for the simultaneous and consistent inclusion of both resonance and off-resonance contributions in the reaction rate calculation. Therefore, to compare with previous works, resonance strengths have been calculated based on the partial widths determined by the R-matrix analysis and are given in Tables III and IV.

While the strengths for the ^{19}F(p, $\alpha_{(2,3,4)}$) ^{16}O reactions are generally consistent, those for the ^{19}F(p, γ) ^{20}Ne reaction are quite discrepant. Except for the resonance at $E_{r,\mathrm{c.m.}}$ = 0.634 MeV, the strength measurements for the other resonances typically differ by more than 2σ. It should be noted that in the NACRE compilation [20] average values were adopted for these strengths, despite the large discrepancies.

G. Direct capture and subthreshold states

Over the energy region that has been accessed by experimental measurement, the ^{19}F(p, γ) ^{20}Ne cross section, at least to the most intense first excited state transition, is dominated

TABLE IV. Comparison of resonance strength measurements for narrow resonances in the ^{19}F(p, $\alpha_{(2,3,4)}$) ^{20}Ne reactions. Note that these resonances strengths only account for the (p, $\alpha_{2,3,4}$) portion of the total cross section at low energies. The uncertainty in the strengths are taken as the systematic uncertainty in the cross-section measurement of Couture *et al.* [30] (16%). Table adopted from Angulo *et al.* [20].

$E_{r,\mathrm{c.m.}}$ (MeV)	E_x (MeV)	J^π	$\omega\gamma$ (eV)					Γ_{p_0} (eV)	Γ_α (eV)	Γ_{total} (eV)
			[72]	[73]	[29]	Others	This work	This work		
0.011	12.855	1^+			8.5×10^{-29}	$7.5(30)\times10^{-29}$ [40]		1.1×10^{-28}[a]	100–1000	100–1000
0.2148(10)	13.0588	2^-		0.022(4)	0.0126(13)		0.015(3)	0.012	1090	1090
0.2279(10)	13.0719	3^-			0.011(4)		0.015(3)	8.6×10^{-4}	87	87
0.3239(10)	13.1679	1^+	37(6)	24(4)	24.3(29)	22.3(8) [70] 22(2) [52] 24(3) [74]	27(5)	35.8[b]	2250	2250
0.4599(10)	13.3039	1^+	10(1)	9(1)	8(1)		9(2)	12.1[b]	822	824
0.5627(10)	13.4067	2^-	52(8)	48(10)	48(7)		67(11)	54	34 600	34 600
0.6345(10)	13.4785	1^+	86(13)	90(14)	75(9)		83(14)	6480	112	6590

[a]Fixed at the central value reported in Kious [41].
[b]Fixed at the central value reported in Couture *et al.* [30].

by resonance transitions through unnatural parity states. However, in Couture *et al.* [30], it was shown that there may be a deep interference minimum at lower energies ($E_{\mathrm{c.m.}} < 200$ keV). The shape of this interference region is highly dependent on assumptions made about background components from the low-energy tails of higher lying resonances, direct capture, and subthreshold state contributions. In particular, direct capture and subthreshold state contributions have seen little experimental investigation.

Only Kious [41] has investigated a possible subthreshold state contribution from a 1^+ level they observed at $E_x = 12.396$ MeV ($S_p = 12.844$ MeV) and only for the (p, α_2) cross section. An example calculation is shown in Fig. 16, where the subthreshold level is given a $\Gamma_{\alpha_2} = 100$ eV ($\theta^2 = 1$) and a proton ANC of 1 fm$^{-1/2}$ ($\theta^2 = 1 \times 10^{-3}$). Here θ^2 is the dimensionless reduced width (see, e.g., Ref. [20]) at the channel radii specified in Table I. These resonance parameters were chosen as they were a combination that gave the maximum value for the $^{19}\mathrm{F}(p, \alpha_2)\,^{16}\mathrm{O}$ S factor at low energy, but still produced a higher-energy cross section that was consistent with data. It can be seen that the subthreshold state can have a significant impact on the cross section. For example, for a nominal temperature of interest of 0.1 GK, the Gamow energy is 120 keV. At this energy, the variation in the S-factor extrapolations, as shown in Fig. 16, is a factor of 17.

V. REACTION RATES

In this section, the rates, and their corresponding upper and lower limits, for the $^{19}\mathrm{F}(p, \gamma)\,^{20}\mathrm{Ne}$ and $^{19}\mathrm{F}(p, \alpha)\,^{16}\mathrm{O}$ reactions are calculated based on the R-matrix extrapolations of the S factors presented in Sec. IV. The rate for the total $^{19}\mathrm{F}(p, \alpha)\,^{16}\mathrm{O}$ reaction is somewhat complicated as it is the sum of the $^{19}\mathrm{F}(p, \alpha_{(0,1,2,3,4)})\,^{16}\mathrm{O}$ reactions. However, the situation is somewhat simplified because the $^{19}\mathrm{F}(p, \alpha_{(0,2)})\,^{16}\mathrm{O}$ reactions dominate. Similarly, it is possible for the $^{19}\mathrm{F}(p, \gamma)\,^{20}\mathrm{Ne}$ reaction to proceed through several different final states, but experimentally the $^{19}\mathrm{F}(p, \gamma_1)\,^{20}\mathrm{Ne}$ transition has been shown to dominate.

Ideally the uncertainty of the reaction rates could be calculated through a detailed Bayesian analysis, but, as highlighted throughout Sec. IV, many of the important level parameters for the near and subthreshold states are either very poorly or completely unknown. Thus, with such incomplete knowledge of the priors, this type of detailed uncertainty analysis does not seem appropriate. Thus the uncertainties that are quoted here should be treated as classical limits, representing estimates of the extreme upper and lower bounds. Therefore, when these rates are utilized in astrophysics calculations that utilize Bayesian uncertainty estimation, it is suggested that the upper and lower limits given here be treated either as the limits of a uniform distribution, or the 3σ values of a normal distribution. The gaps in the experimental data highlighted in this work should serve as motivation for new experimental studies, making a more detailed Bayesian uncertainty analysis of this reaction on the horizon.

The individual reaction rates and the upper and lower limits for the dominate components are given in Table V. The total reaction rates are then presented in Table VI. The following sections give further details on how each of the reaction rate components were calculated.

A. $^{19}\mathrm{F}(p, \alpha_0)\,^{16}\mathrm{O}$ rate

There have been several recent investigations of the $^{19}\mathrm{F}(p, \alpha_0)\,^{16}\mathrm{O}$ component of the reaction rate. Measurements of the $^{19}\mathrm{F}(p, \alpha_0)\,^{16}\mathrm{O}$ cross section via THM resulted in updated rates as reported in LaCognata *et al.* [33]. The rate was then revised in LaCognata *et al.* [34] based on the new direct measurements of Lombardo *et al.* [32]. New measurements were then made by Indelicato *et al.* [35] reporting the most recent version of the rate based on THM data. Most recently, Lombardo *et al.* [44] has reported a revised rate for the $^{19}\mathrm{F}(p, \alpha_0)\,^{16}\mathrm{O}$ and $^{19}\mathrm{F}(p, \alpha_1)\,^{16}\mathrm{O}$ components based on a comprehensive R-matrix analysis that extends to high energies. Both the new THM measurements [33,35] and the direct measurements of Lombardo *et al.* [32] indicate a larger $^{19}\mathrm{F}(p, \alpha_0)\,^{16}\mathrm{O}$ reaction rate than that of older works (in particular of Lorenz-Wirzba [24]), based on the observation of new resonances in the low-energy region. In the present work, previous literature data have been reinvestigated, which show only a flat low-energy cross section without resonant enhancement. This generally agrees with the previous results of Angulo *et al.* [20], which considered mainly the same data sets.

Therefore, the uncertainty range for this component of the reaction rate takes the $^{19}\mathrm{F}(p, \alpha_0)\,^{16}\mathrm{O}$ rate from Lombardo *et al.* [44] as an upper limit and takes the rate of the present analysis as a lower limit. Uncertainties due to the overall normalization of experimental data, which are interpreted to be constant in energy, are also included (see Sec. IV E).

B. $^{19}\mathrm{F}(p, \alpha_1)\,^{16}\mathrm{O}$ rate

A revised rate for the $^{19}\mathrm{F}(p, \alpha_1)\,^{16}\mathrm{O}$ reaction has been presented in Lombardo *et al.* [44], where an enhancement has been indicated due to the presence of a broad 2^+ resonance. The rate presented in Lombardo *et al.* [44] is consistent with that found in the present analysis. While there is significant enhancement, the contribution is still less than the $^{19}\mathrm{F}(p, \alpha_0)\,^{16}\mathrm{O}$ rate contribution at all temperatures. This revised rate has been adopted here.

C. $^{19}\mathrm{F}(p, \alpha_{(2,3,4)})\,^{16}\mathrm{O}$ rates

One of the main focuses of this work has been a re-evaluation of the $^{19}\mathrm{F}(p, \alpha_{(2,3,4)})\,^{16}\mathrm{O}$ components of the reaction rate. The data shown that $^{19}\mathrm{F}(p, \alpha_2)\,^{16}\mathrm{O}$ reaction dominates over the entire low-energy range for these three reaction components. One of the main results of this work is the demonstration that interference with the 1^+ threshold state and subthreshold state can produce a significant enhancement in the $^{19}\mathrm{F}(p, \alpha_2)\,^{16}\mathrm{O}$ cross section below the lowest-energy observed resonance. With this

TABLE V. Recommended rates (rec) for the ^{19}F(p, $\alpha_{(2,3,4)}$) ^{16}O and ^{19}F(p, γ_1) ^{20}Ne reactions as well as a lower limit (low) for the ^{19}F(p, α_0) ^{16}O and lower and upper rate limits (upper) for the ^{19}F(p, α_2) ^{16}O and ^{19}F(p, γ_1) ^{20}Ne reactions. See text for details.

T	(p, α_0) (low)	(p, α_2) (rec)	(p, α_2) (low)	(p, α_2) (up)	(p, α_3)	(p, α_4)	(p, γ_1) (rec)	(p, γ_1) (low)	(p, γ_1) (up)
(GK)	($cm^3 mole^{-1} s^{-1}$)								
0.01	1.66×10^{-24}	4.99×10^{-23}	3.74×10^{-23}	5.73×10^{-23}	4.01×10^{-29}	1.73×10^{-28}	1.10×10^{-28}	1.89×10^{-30}	6.18×10^{-27}
0.02	3.60×10^{-17}	2.20×10^{-16}	1.65×10^{-16}	3.03×10^{-16}	1.10×10^{-21}	4.95×10^{-21}	2.38×10^{-21}	4.13×10^{-23}	3.53×10^{-20}
0.03	1.27×10^{-13}	3.53×10^{-13}	2.65×10^{-13}	5.77×10^{-13}	4.74×10^{-18}	2.23×10^{-17}	8.44×10^{-18}	1.47×10^{-19}	7.04×10^{-17}
0.04	2.17×10^{-11}	3.51×10^{-11}	2.64×10^{-11}	6.77×10^{-11}	9.81×10^{-16}	4.77×10^{-15}	1.44×10^{-15}	2.51×10^{-17}	8.70×10^{-15}
0.05	8.36×10^{-10}	8.85×10^{-10}	6.64×10^{-10}	2.01×10^{-9}	4.53×10^{-14}	2.27×10^{-13}	5.57×10^{-14}	9.64×10^{-16}	3.43×10^{-13}
0.06	1.35×10^{-8}	9.97×10^{-9}	7.48×10^{-9}	2.69×10^{-8}	8.77×10^{-13}	4.49×10^{-12}	8.98×10^{-13}	1.54×10^{-14}	5.67×10^{-12}
0.07	1.24×10^{-7}	6.66×10^{-8}	5.00×10^{-8}	2.15×10^{-7}	9.96×10^{-12}	5.05×10^{-11}	8.25×10^{-12}	1.44×10^{-13}	5.36×10^{-11}
0.08	7.67×10^{-7}	3.13×10^{-7}	2.35×10^{-7}	1.21×10^{-6}	9.31×10^{-11}	3.88×10^{-10}	5.15×10^{-11}	1.11×10^{-12}	3.44×10^{-10}
0.09	3.58×10^{-6}	1.20×10^{-6}	8.97×10^{-7}	5.29×10^{-6}	9.46×10^{-10}	2.31×10^{-9}	2.46×10^{-10}	1.06×10^{-11}	1.67×10^{-9}
0.1	1.35×10^{-5}	4.50×10^{-6}	3.37×10^{-6}	1.98×10^{-5}	9.00×10^{-9}	1.17×10^{-8}	9.93×10^{-10}	1.03×10^{-10}	6.58×10^{-9}
0.15	1.44×10^{-3}	3.87×10^{-3}	2.90×10^{-3}	5.62×10^{-3}	1.88×10^{-5}	2.20×10^{-5}	3.36×10^{-7}	2.41×10^{-7}	1.43×10^{-6}
0.2	2.69×10^{-2}	4.55×10^{-1}	3.41×10^{-1}	4.96×10^{-1}	1.83×10^{-3}	5.49×10^{-3}	2.78×10^{-5}	2.60×10^{-5}	1.31×10^{-4}
0.3	1.04×10^{0}	9.98×10^{1}	7.49×10^{1}	1.02×10^{2}	3.71×10^{-1}	1.51×10^{0}	5.63×10^{-3}	5.56×10^{-3}	2.80×10^{-2}
0.4	1.03×10^{1}	1.45×10^{3}	1.09×10^{3}	1.46×10^{3}	5.65×10^{0}	2.35×10^{1}	8.99×10^{-2}	8.92×10^{-2}	4.11×10^{-1}
0.5	5.25×10^{1}	6.82×10^{3}	5.12×10^{3}	6.81×10^{3}	2.96×10^{1}	1.21×10^{2}	6.04×10^{-1}	6.01×10^{-1}	2.32×10^{0}
0.6	1.83×10^{2}	1.86×10^{4}	1.39×10^{4}	1.84×10^{4}	9.74×10^{1}	3.68×10^{2}	2.90×10^{0}	2.89×10^{0}	8.43×10^{0}
0.7	5.02×10^{2}	3.73×10^{4}	2.80×10^{4}	3.69×10^{4}	2.71×10^{2}	8.32×10^{2}	1.04×10^{1}	1.04×10^{1}	2.36×10^{1}
0.8	1.15×10^{3}	6.24×10^{4}	4.68×10^{4}	6.15×10^{4}	7.01×10^{2}	1.58×10^{3}	2.88×10^{1}	2.87×10^{1}	5.56×10^{1}
0.9	2.32×10^{3}	9.30×10^{4}	6.97×10^{4}	9.12×10^{4}	1.66×10^{3}	2.68×10^{3}	6.41×10^{1}	6.39×10^{1}	1.14×10^{2}
1	4.19×10^{3}	1.28×10^{5}	9.59×10^{4}	1.25×10^{5}	3.54×10^{3}	4.20×10^{3}	1.21×10^{2}	1.21×10^{2}	2.10×10^{2}

enhancement the ^{19}F(p, α_2) ^{16}O reaction component could even overshadow the ^{19}F(p, α_0) ^{16}O reaction component in the low-temperature range where it has traditionally been assumed to dominate.

D. ^{19}F(p, α) ^{16}O total rate

The total ^{19}F(p, α) ^{16}O rate is dominated by the ^{19}F(p, α_0) ^{16}O and ^{19}F(p, α_2) ^{16}O reactions. For the central value of the rate, the threshold and subthreshold states are not

TABLE VI. Recommended rates (rec) for the total ^{19}F(p, α) ^{16}O and ^{19}F(p, γ) ^{20}Ne reactions as well as lower limit (low) and upper limits (upper) See text for details.

T	(p, α) (rec)	(p, α) (low)	(p, α) (upper)	(p, γ) (rec)	(p, γ) (low)	(p, γ) (upper)
(GK)	($cm^3 mole^{-1} s^{-1}$)					
0.01	1.77×10^{-24}	1.33×10^{-24}	5.90×10^{-23}	1.10×10^{-28}	1.89×10^{-30}	6.18×10^{-27}
0.02	3.78×10^{-17}	2.84×10^{-17}	3.40×10^{-16}	2.38×10^{-21}	4.13×10^{-23}	3.53×10^{-20}
0.03	1.34×10^{-13}	1.01×10^{-13}	7.07×10^{-13}	8.44×10^{-18}	1.47×10^{-19}	7.04×10^{-17}
0.04	2.30×10^{-11}	1.73×10^{-11}	8.99×10^{-11}	1.44×10^{-15}	2.51×10^{-17}	8.70×10^{-15}
0.05	8.87×10^{-10}	6.65×10^{-10}	2.87×10^{-9}	5.57×10^{-14}	9.64×10^{-16}	3.43×10^{-13}
0.06	1.43×10^{-8}	1.07×10^{-8}	4.12×10^{-8}	8.98×10^{-13}	1.54×10^{-14}	5.67×10^{-12}
0.07	1.31×10^{-7}	9.79×10^{-8}	3.53×10^{-7}	8.25×10^{-12}	1.44×10^{-13}	5.36×10^{-11}
0.08	8.13×10^{-7}	6.10×10^{-7}	2.07×10^{-6}	5.15×10^{-11}	1.11×10^{-12}	3.44×10^{-10}
0.09	3.91×10^{-6}	2.93×10^{-6}	9.24×10^{-6}	2.46×10^{-10}	1.06×10^{-11}	1.67×10^{-9}
0.1	1.62×10^{-5}	1.22×10^{-5}	3.42×10^{-5}	9.93×10^{-10}	1.03×10^{-10}	6.58×10^{-9}
0.15	5.58×10^{-3}	5.24×10^{-3}	8.73×10^{-3}	3.36×10^{-7}	2.41×10^{-7}	1.43×10^{-6}
0.2	4.95×10^{-1}	3.95×10^{-1}	6.58×10^{-1}	2.78×10^{-5}	2.60×10^{-5}	1.31×10^{-4}
0.3	9.73×10^{1}	7.30×10^{1}	1.22×10^{2}	5.63×10^{-3}	5.56×10^{-3}	2.80×10^{-2}
0.4	1.39×10^{3}	1.04×10^{3}	1.74×10^{3}	8.99×10^{-2}	8.92×10^{-2}	4.11×10^{-1}
0.5	6.58×10^{3}	4.93×10^{3}	8.22×10^{3}	6.04×10^{-1}	6.01×10^{-1}	2.32×10^{0}
0.6	1.81×10^{4}	1.36×10^{4}	2.26×10^{4}	2.90×10^{0}	2.89×10^{0}	8.43×10^{0}
0.7	3.70×10^{4}	2.77×10^{4}	4.62×10^{4}	1.04×10^{1}	1.04×10^{1}	2.36×10^{1}
0.8	6.39×10^{4}	4.79×10^{4}	7.99×10^{4}	2.88×10^{1}	2.87×10^{1}	5.56×10^{1}
0.9	9.96×10^{4}	7.47×10^{4}	1.25×10^{5}	6.41×10^{1}	6.39×10^{1}	1.14×10^{2}
1	1.41×10^{5}	1.09×10^{5}	1.82×10^{5}	1.21×10^{2}	1.21×10^{2}	2.10×10^{2}

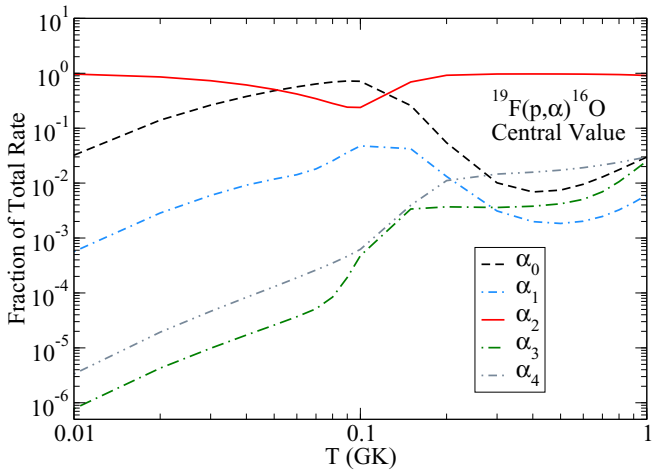

FIG. 18. Fractional contributions of the different final state contributions to the central value calculation of $^{19}\mathrm{F}(p,\alpha)\,^{16}\mathrm{O}$ reaction rate. Here the $^{19}\mathrm{F}(p,\alpha_0)\,^{16}\mathrm{O}$ rate dominates around $T \approx 0.1$ GK, as found in previous works (e.g., NACRE [20]).

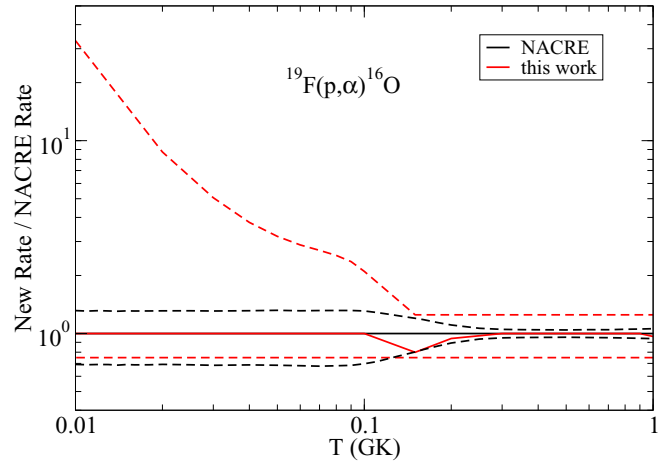

FIG. 20. Ratio of the present reaction $^{19}\mathrm{F}(p,\alpha)\,^{16}\mathrm{O}$ reaction rate to that of the NACRE compilation [20] (red solid line). The upper and lower uncertainty limits are indicated by the red dashed lines (this work) and the black dashed lines (NACRE [20]).

included in the $^{19}\mathrm{F}(p,\alpha_2)\,^{16}\mathrm{O}$ component. This fit is nearly identical to that presented in Couture *et al.* [30] and is also equivalent over the temperature range under investigation to the narrow width ($\Gamma = 2$ eV) solution shown in Fig. 16. Figure 18 shows the fractional contribution to the total rate of the different reaction channels for the central value rate.

For the upper limit, the interference solution shown by the black line in Fig. 16 is used, where both a broad width is taken for the threshold level ($\Gamma = 1$ keV) and a subthreshold contribution is included. This enhanced $^{19}\mathrm{F}(p,\alpha_2)\,^{16}\mathrm{O}$ cross section is now larger than even the resonance enhanced rates of the $^{19}\mathrm{F}(p,\alpha_0)\,^{16}\mathrm{O}$ cross section reported in recent works [35,44] (as discussed in Sec. V A). The fraction of the total rate stemming from the different reactions is given in Fig. 19.

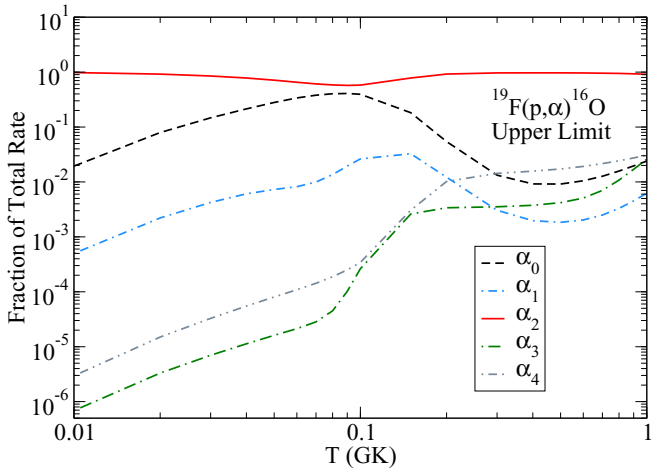

FIG. 19. Fractional contributions of the different final state contributions to the upper limit calculation of $^{19}\mathrm{F}(p,\alpha)\,^{16}\mathrm{O}$ reaction rate. In this case the interference of the threshold state and subthreshold resonances enhance the $^{19}\mathrm{F}(p,\alpha_2)\,^{16}\mathrm{O}$ reaction, making it dominant at all temperatures.

The rate and the recommended uncertainty range are shown in Fig. 20.

E. $^{19}\mathrm{F}(p,\gamma)\,^{20}\mathrm{Ne}$ reaction rate

One of the other main results of this work has been a re-analysis of the $^{19}\mathrm{F}(p,\gamma)\,^{20}\mathrm{Ne}$ reaction rate. Here the previous experimental results of Kious [41], Spyrou *et al.* [29], and Couture *et al.* [30] are combined in a global *R*-matrix analysis to gain more insight into the extrapolation of the low-energy cross section. In Angulo *et al.* [20], a 50% uncertainty was adopted for the low-temperature range for the $^{19}\mathrm{F}(p,\gamma)\,^{20}\mathrm{Ne}$ reaction. Here it has been shown that, through previously neglected interference, the near threshold state and direct capture can result in considerably larger uncertainties, becoming about an order of magnitude at $T = 0.1$ GK and larger than three orders of magnitude at very low temperatures (see Sec. IV and Fig. 21). The effects of this larger uncertainty range are investigated in Sec. VI.

VI. ASTROPHYSICAL IMPACT

The details of the suggested CNO breakout in massive Pop III stars are discussed in Clarkson and Herwig [19]. Here we will repeat the most salient points and refer the reader to that work for further details.

Pop III stars begin their lives with primordial composition and begin hydrogen burning via *p*-*p* chains and contract until central temperatures are high enough ($\approx 10^8$ K) to ignite the 3α-process. This bridges the mass 5 and mass 8 gaps, such that a small amount of CNO catalyst is formed [75], $X_{^{12}\mathrm{C}} \approx 10^{-9}$, which kickstarts the CNO cycle. In Clarkson and Herwig [19], 1D stellar evolution simulations showed that hot CNO cycling takes place at peak core H-burning temperatures although this phase lasts for $\approx 1\%$ of the total main-sequence lifetime. Hot CNO cycles can be activated for a short period of time at the end of hydrogen shell burning in these stars as well. Single-zone nucleosynthesis calculations revealed that small amounts

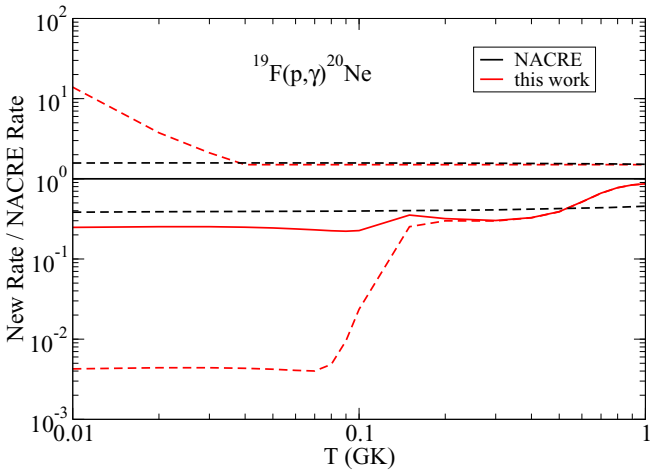

FIG. 21. Ratio of the present reaction ^{19}F(p, γ) ^{20}Ne reaction rate to that of the NACRE compilation [20] (red solid line). The upper and lower uncertainty limits are indicated by the red dashed lines (this work) and the black dashed lines (NACRE [20]).

of Ca ($X_{Ca} \approx 10^{-12}$) are produced through breakout reactions passing through ^{19}F.

To determine the impact of the presented revisions of the ^{19}F(p, α) ^{16}O and ^{19}F(p, γ) ^{20}Ne reaction rates, we have run single-zone simulations with the same conditions as those adopted in Clarkson and Herwig [19], which use a constant temperature, $T = 1.19 \times 10^8$ K, and density, $\rho = 39.8 \mathrm{g\,cm^{-3}}$, based on their 80 $M_\odot$, Pop III stellar evolution model. Initial abundances are those attributed to the Big Bang abundances [76]. We use the NuGrid collaboration's PPN code [77] with charged-particle reactions from the JINA reaclib V0.5 [78] and ^{19}F $+p$ reactions taken from the NACRE compilation [20], with symmetric uncertainties of 50% as provided. The abundances presented here are measured at the time step where the mass fraction of hydrogen is 10^{-2}. Other single zone calculations using slightly different temperature and density conditions presented in Clarkson and Herwig [19] were also tested with the updated reaction rates but no notable differences in the findings presented below were found.

These simulations show that the new recommended values for these rates decrease the abundances of species with $Z > 9$ (Fig. 22). Mass fractions for these species are quite small in both simulations, with ^{40}Ca being the most abundant, followed by ^{32}S and ^{28}Si. All other mass fractions are $<10^{-15}$. The updated reaction rates lead to a change of ≈70% in these species. Similarly, Fig. 23 shows the change in abundance evolution in our single zone simulations.

Figure 24 shows the mass fractions of Ca, and the sum of all isotopes with $Z > 9$ in these simulations. The change in abundance is due almost entirely to the revision of the ^{19}F(p, γ) ^{20}Ne reaction rate. The larger uncertainty stems from the investigation of additional uncharacterized reaction contributions to the low-energy cross section, namely, direct capture, a near threshold state, and subthreshold states (see Secs. IV B and IV G). In the NACRE compilation [20], a nonresonant component was considered, where an estimated uncertainty of 50% was adopted. The total mass fraction of Ca is 2×10^{-13} with the rates presented in this work, and 6.5×10^{-13} using the NACRE rates [20]. Clarkson and Herwig [19] found Ca mass fractions of ≈10^{-12} in 1D stellar evolution models, somewhat more than what is found in single zone calculations. The difference here is due to the fact that 1D models take into account the continued convective mixing and supply of additional seed CNO material, which is not included in the one-zone simulation. Therefore, the one-zone simulations must be interpreted in a differential sense, i.e., the numbers presented here are not intended to be compared with

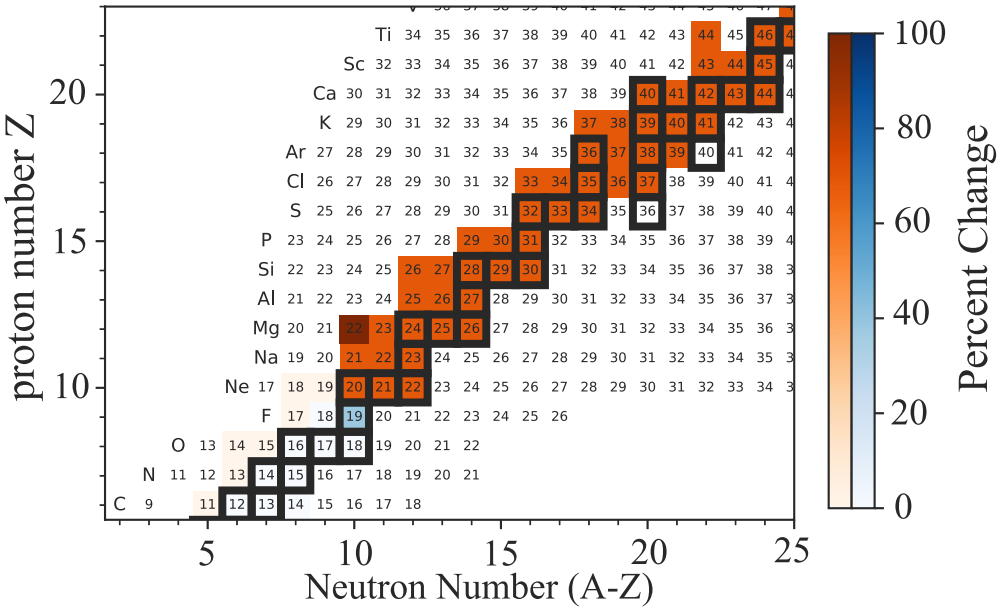

FIG. 22. Abundance chart showing the percent change of isotopes using updated ^{19}F $+p$ reaction rates, presented in this work, compared to rates from the NACRE compilation [20]. Orange colors indicate a reduction in the total mass fractions and blue indicates an increase.

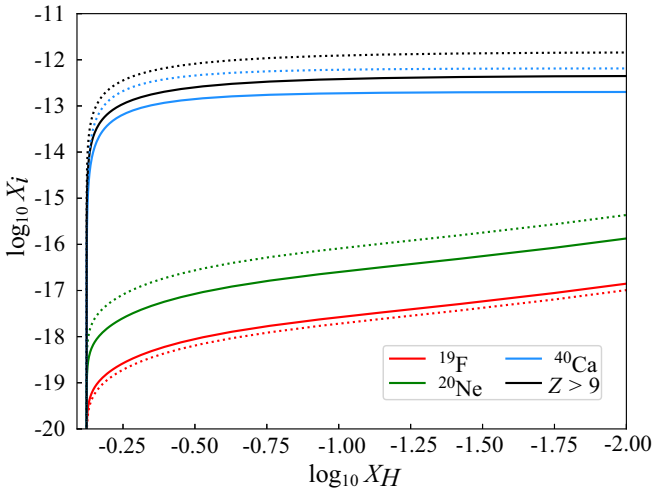

FIG. 23. Abundance evolution showing simulations with rates from this work (solid lines) and using rates from the NACRE compilation [20] for ^{19}F$+p$ reactions (dotted lines). Abundances are plotted as a function of the decreasing amount of H in the single-zone network simulation. Therefore time proceeds from left to right.

stellar observations directly, but rather show the magnitude of the impact.

As explained in the Introduction, Clarkson and Herwig [19] found that model predictions of Ca from H burning sources are ≈0.8 to 2 dex too low to account for the observed Ca abundances in the most Fe-poor stars. Repeating the same analysis with the updated reaction rates presented here would increase this tension as the predicted Ca range from H burning decreases by ≈0.5 dex. With the updated rates, the models and methods of Clarkson and Herwig [19] would predict H-burning Ca abundances lower by 1.3 to 2.5 dex compared to observations. However, within the range of nuclear uncertainty the predicted Ca abundance approaches the observed Ca abundance within 0.5 dex. More accurate nuclear data is needed to determine the origin of Ca in Pop III stars and thereby distinguish between the faint supernova model and alternative models, such as the light *i*-process model proposed by Clarkson *et al.* [21], or explosive burning [79].

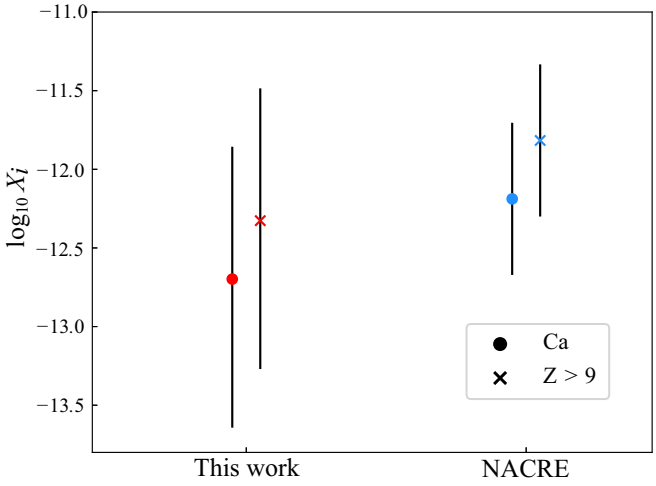

FIG. 24. Mass fractions of Ca, and all isotopes with $Z > 9$ in a Pop III hydrogen burning single zone simulation, calculated using either the ^{19}F$+p$ reaction rates of this work (red) or those from the NACRE compilation [20] (blue). Bars indicate the variation of these abundances within the uncertainties.

To summarize, to estimate the upper limit of Ca production in the most Fe-poor stars a faint-supernova model has been suggested that requires the fall-back of Ca produced from Si burning, i.e., the Ca produced in these models is not produced during the explosion, and comes from the star's outermost layers. Based on their stellar evolution simulations Clarkson and Herwig [19] find, under these assumptions, an upper limit [Ca/H] $= -7.7$, about 0.8 dex below the measured value for the Keller star. The new ^{19}F rates presented here lower the predicted Ca abundance by ≈70% at the temperatures present in Pop III H burning (100–150 MK). However, because the uncertainty in the ^{19}F reactions rates is found to be much larger than previously estimated, the updated calculations remain consistent with previous results, clearly indicating the need for additional nuclear data.

VII. SUMMARY

A comprehensive *R*-matrix analysis has been performed that includes the majority of the low-energy cross-section data for ^{19}F$+p$ reactions using the phenomenological *R*-matrix approach. The simultaneous fit was able to satisfactorily reproduce the available cross-section data for the $^{19}\mathrm{F}(p,\alpha)^{16}\mathrm{O}$, $^{19}\mathrm{F}(p,\gamma)^{20}$, and $^{19}\mathrm{F}(p,p)^{19}\mathrm{F}$ data. As several recent works have focused on the $^{19}\mathrm{F}(p,\alpha_{(0,1)})^{16}\mathrm{O}$ reaction, the present work centers on the $^{19}\mathrm{F}(p,\alpha_{(2,3,4)})^{16}\mathrm{O}$ and $^{19}\mathrm{F}(p,\gamma)^{20}$ reactions. In general, a similar range of uncertainty is found for the $^{19}\mathrm{F}(p,\alpha)^{16}\mathrm{O}$ reaction rate, but it is found that the $^{19}\mathrm{F}(p,\alpha_2)^{16}\mathrm{O}$ cross section may be comparable in strength with the $^{19}\mathrm{F}(p,\alpha_0)^{16}\mathrm{O}$ cross section, even at low energies where traditionally the $^{19}\mathrm{F}(p,\alpha_0)^{16}\mathrm{O}$ cross section has been thought to dominate the total cross section. It is also found that the uncertainty in the low-energy cross section of the $^{19}\mathrm{F}(p,\gamma)^{20}$ reaction is considerably larger than previously estimated (e.g., NACRE [20]).

These results indicate that further measurements are needed. Of prime importance, proton transfer studies should be made to determine the proton ANCs of proton bound states. These are needed both to constrain contributions from subthreshold states and to determine the magnitude of the direct capture contributions for the capture reaction. Measurement of the α_2-width of the near threshold state is also also critical. Low-energy measurements of the $^{19}\mathrm{F}(p,p_{(1,2)})^{19}\mathrm{F}$ reactions are also highly desirable to better constrain the multichannel *R*-matrix analysis. As pointed out in Couture *et al.* [30], $^{19}\mathrm{F}(p,\gamma_1)^{20}\mathrm{Ne}$ cross section should be measured to higher energies to better constrain high energy resonances contributions. Finally, but likely the most difficult, the $^{19}\mathrm{F}(p,\alpha_2)^{16}\mathrm{O}$ and $^{19}\mathrm{F}(p,\gamma)^{20}$ cross-section measurements need to be extended to lower energies, in particular, in their off-resonance regions, to limit the many different interference solutions that are currently possible. In particular, if measurements and uncertainties for the bound state and near threshold levels can

be made, a more rigorous uncertainty analysis will then be appropriate, leading to more statistically meaningful reaction rate uncertainties.

The larger uncertainty found for the ^{19}F(p, γ) ^{20}Ne reaction only goes to further emphasize the resulting uncertainty in nucleosynthesis calculations where these rates are needed. The new recommended ^{19}F(p, γ) ^{20}Ne rate of this work reduces the mass fractions for elements with $Z > 9$ during hydrogen burning in massive Population III stars, thus increasing the difficulty in creating Ca solely within hydrogen burning conditions in the first stars.

ACKNOWLEDGMENTS

This research utilized resources from the Notre Dame Center for Research Computing and was supported by the National Science Foundation through Grant No. Phys-2011890, and the Joint Institute for Nuclear Astrophysics through Grant No. PHY-1430152 (JINA Center for the Evolution of the Elements). F.H. acknowledges funding through a NSERC Discovery Grant. This research has used the Astrohub online virtual research environment [80] developed and operated by the Computational Stellar Astrophysics group [81] at the University of Victoria and hosted on the Computed Canada Arbutus Cloud at the University of Victoria. I.L. acknowledges the support of the INFN SyLiNuRe grant. A.C. acknowledges support from the US Department of Energy (Contract No. 89233218CNA000001) by the Laboratory Directed Research and Development program of Los Alamos National Laboratory under Project No. LDRD-DR-20190021DR.

[1] M. Wiescher, J. Görres, and H. Schatz, Breakout reactions from the CNO cycles, J. Phys. G: Nucl. Part. Phys. **25**, R133 (1999).

[2] K. Langanke, M. Wiescher, W. A. Fowler, and J. Gorres, A new estimate of the ^{19}Ne(p, γ)^{20}Na and ^{15}O(α, γ)^{19}Ne reaction rates at stellar energies, Astrophys. J. **301**, 629 (1986).

[3] W. P. Tan, J. L. Fisker, J. Görres, M. Couder, and M. Wiescher, ^{15}O(α, γ) ^{19}Ne Breakout Reaction and Impact on x-Ray Bursts, Phys. Rev. Lett. **98**, 242503 (2007).

[4] W. P. Tan, J. Görres, M. Beard, M. Couder, A. Couture, S. Falahat, J. L. Fisker, L. Lamm, P. J. LeBlanc, H. Y. Lee, S. O'Brien, A. Palumbo, E. Stech, E. Strandberg, and M. Wiescher, Measurement of the decay branching ratios of the α-unbound states in ^{19}Ne and the ^{15}O(α, γ) reaction rate, Phys. Rev. C **79**, 055805 (2009).

[5] M. R. Hall, D. W. Bardayan, T. Baugher, A. Lepailleur, S. D. Pain, A. Ratkiewicz, S. Ahn, J. M. Allen, J. T. Anderson, A. D. Ayangeakaa, J. C. Blackmon, S. Burcher, M. P. Carpenter, S. M. Cha, K. Y. Chae, K. A. Chipps, J. A. Cizewski, M. Febbraro, O. Hall, J. Hu, C. L. Jiang, K. L. Jones, E. J. Lee, P. D. O'Malley, S. Ota, B. C. Rasco, D. Santiago-Gonzalez, D. Seweryniak, H. Sims, K. Smith, W. P. Tan, P. Thompson, C. Thornsberry, R. L. Varner, D. Walter, G. L. Wilson, and S. Zhu, New γ-ray transitions observed in ^{19}Ne with implications for the ^{15}O(α, γ) ^{19}Ne reaction rate, Phys. Rev. C **99**, 035805 (2019).

[6] D. Torresi, C. Wheldon, T. Kokalova, S. Bailey, A. Boiano, C. Boiano, M. Fisichella, M. Mazzocco, C. Parascandolo, D. Pierroutsakou, E. Strano, M. Zadro, M. Cavallaro, S. Cherubini, N. Curtis, A. Di Pietro, J. P. Fernández Garcia, P. Figuera, T. Glodariu, J. Gręboszz, M. La Cognata, M. La Commara, M. Lattuada, D. Mengoni, R. G. Pizzone, C. Signorini, C. Stefanini, L. Stroe, and C. Spitaleri, Evidence for ^{15}O $+\alpha$ resonance structures in ^{19}Ne via direct measurement, Phys. Rev. C **96**, 044317 (2017).

[7] C. Wrede, B. E. Glassman, D. Pérez-Loureiro, J. M. Allen, D. W. Bardayan, M. B. Bennett, B. A. Brown, K. A. Chipps, M. Febbraro, C. Fry, M. R. Hall, O. Hall, S. N. Liddick, P. O'Malley, W.-J. Ong, S. D. Pain, S. B. Schwartz, P. Shidling, H. Sims, P. Thompson, and H. Zhang, New portal to the ^{15}**O**(α, γ) ^{19}**Ne** resonance triggering CNO-cycle breakout, Phys. Rev. C **96**, 032801(R) (2017).

[8] W. Bradfield-Smith, T. Davinson, A. DiPietro, A. M. Laird, A. N. Ostrowski, A. C. Shotter, P. J. Woods, S. Cherubini, W. Galster, J. S. Graulich, P. Leleux, L. Michel, A. Ninane, J. Vervier, J. Görres, M. Wiescher, J. Rahighi, and J. Hinnefeld, Breakout from the hot CNO cycle via the ^{18}Ne(α, p)^{21}Na reaction, Phys. Rev. C **59**, 3402 (1999).

[9] A. Matic, A. M. vandenBerg, M. N. Harakeh, H. J. Wörtche, G. P. A. Berg, M. Couder, J. L. Fisker, J. Görres, P. LeBlanc, S. O'Brien, M. Wiescher, K. Fujita, K. Hatanaka, Y. Sakemi, Y. Shimizu, Y. Tameshige, A. Tamii, M. Yosoi, T. Adachi, Y. Fujita, Y. Shimbara, H. Fujita, T. Wakasa, P. O. Hess, B. A. Brown, and H. Schatz, High-precision (p, t) reaction measurement to determine ^{18}Ne(α, p)^{21}Na reaction rates, Phys. Rev. C **80**, 055804 (2009).

[10] L. Y. Zhang, J. J. He, A. Parikh, S. W. Xu, H. Yamaguchi, D. Kahl, S. Kubono, P. Mohr, J. Hu, P. Ma, S. Z. Chen, Y. Wakabayashi, H. W. Wang, W. D. Tian, R. F. Chen, B. Guo, T. Hashimoto, Y. Togano, S. Hayakawa, T. Teranishi, N. Iwasa, T. Yamada, T. Komatsubara, Y. H. Zhang, and X. H. Zhou, Investigation of the thermonuclear ^{18}Ne(α, p)^{21}Na reaction rate via resonant elastic scattering of ^{21}Na $+p$, Phys. Rev. C **89**, 015804 (2014).

[11] P. J. C. Salter, M. Aliotta, T. Davinson, H. Al Falou, A. Chen, B. Davids, B. R. Fulton, N. Galinski, D. Howell, G. Lotay, P. Machule, A. S. Murphy, C. Ruiz, S. Sjue, M. Taggart, P. Walden, and P. J. Woods, Measurement of the ^{18}Ne(α, p_0)^{21}Na Reaction Cross Section in the Burning Energy Region for x-Ray Bursts, Phys. Rev. Lett. **108**, 242701 (2012).

[12] K. Y. Chae, D. W. Bardayan, J. C. Blackmon, K. A. Chipps, R. Hatarik, K. L. Jones, R. L. Kozub, J. F. Liang, C. Matei, B. H. Moazen, C. D. Nesaraja, P. D. O'Malley, S. D. Pain, S. T. Pittman, and M. S. Smith, Constraint on the astrophysical ^{18}Ne(α, p)^{21}Na reaction rate through a ^{24}Mg(p, t)^{22}Mg measurement, Phys. Rev. C **79**, 055804 (2009).

[13] A. Frebel and J. E. Norris, Near-field cosmology with extremely metal-poor stars, Annu. Rev. Astron. Astrophys. **53**, 631 (2015).

[14] S. C. Keller, M. S. Bessell, A. Frebel, A. R. Casey, M. Asplund, H. R. Jacobson, K. Lind, J. E. Norris, D. Yong, A. Heger, Z. Magic, G. S. da Costa, B. P. Schmidt, and P. Tisserand, A single low-energy, iron-poor supernova as the source of metals in the star SMSS J031300.36-670839.3, Nature (London) **506**, 463 (2014).

[15] T. Nordlander, A. M. Amarsi, K. Lind, M. Asplund, P. S. Barklem, A. R. Casey, R. Collet, and J. Leenaarts, 3D NLTE analysis of the most iron-deficient star, SMSS0313-6708, Astron. Astrophys. **597**, A6 (2017).

[16] M. Asplund, N. Grevesse, A. J. Sauval, and P. Scott, The chemical composition of the sun, Annu. Rev. Astron. Astrophys. **47**, 481 (2009).

[17] K. Takahashi, H. Umeda, and T. Yoshida, Stellar yields of rotating first stars. I. yields of weak supernovae and abundances of carbon-enhanced hyper-metal-poor stars, Astrophys. J. **794**, 40 (2014).

[18] R. Collet, M. Asplund, and R. Trampedach, The chemical compositions of the extreme halo stars HE 0107-5240 and HE 1327-2326 inferred from three-dimensional hydrodynamical model atmospheres, Astrophys. J. **644**, L121 (2006).

[19] O. Clarkson and F. Herwig, Convective H-He interactions in massive population III stellar evolution models, Mon. Not. R. Astron. Soc. **500**, 2685 (2020).

[20] C. Angulo, M. Arnould, M. Rayet, P. Descouvemont, D. Baye, C. Leclercq-Willain, A. Coc, S. Barhoumi, P. Aguer, C. Rolfs, R. Kunz, J. Hammer, A. Mayer, T. Paradellis, S. Kossionides, C. Chronidou, K. Spyrou, S. Degl'Innocenti, G. Fiorentini, B. Ricci, S. Zavatarelli, C. Providencia, H. Wolters, J. Soares, C. Grama, J. Rahighi, A. Shotter, and M. L. Rachti, A compilation of charged-particle induced thermonuclear reaction rates, Nucl. Phys. A **656**, 3 (1999).

[21] O. Clarkson, F. Herwig, and M. Pignatari, Pop III I. Process nucleosynthesis and the elemental abundances of SMSS J0313-6708 and the most iron-poor stars, Mon. Not. R. Astron. Soc. **474**, L37 (2018).

[22] M. Freer, H. Horiuchi, Y. Kanada-En'yo, D. Lee, and Ulf-G. Meißner, Microscopic clustering in light nuclei, Rev. Mod. Phys. **90**, 035004 (2018).

[23] G. R. Caughlan and W. A. Fowler, Thermonuclear reaction rates V, At. Data Nucl. Data Tables **40**, 283 (1988).

[24] H. Lorenz-Wirzba, Untersuchung von (p,α) Reaktionen Unterhalb der Coulombbarriere, Ph.D. thesis, Westfälischen Wilhelms-Universität zu Münster, 1978.

[25] H. Herndl, H. Abele, G. Staudt, B. Bach, K. Grün, H. Scsribany, H. Oberhummer, and G. Raimann, Direct reaction analysis of $^{19}\mathrm{F}(p,\alpha)^{16}\mathrm{O}$ below the Coulomb barrier, Phys. Rev. C **44**, R952 (1991).

[26] R. Ott, Die Astrophysikalischen Reaktionsraten der Reaktionen $^{19}F(p,\alpha)^{16}0$ und $^{19}F(p,\gamma_1)^{20}$Ne, Ph.D. thesis, Institut für Strahlenphysik der Universität Stuttgart, 1997.

[27] S. Dababneh, K. Toukan, and I. Khubeis, Excitation function of the nuclear reaction $^{19}\mathrm{F}(p,\alpha\gamma)^{16}\mathrm{O}$ in the proton energy range 0.3–3.0 MeV, Nucl. Instrum. Methods Phys. Res. Sec. B: Beam Interact. Mater. Atoms **83**, 319 (1993).

[28] K. Spyrou, C. Chronidou, S. Harissopulos, S. Kossionides, and T. Paradellis, Cross section and resonance strengths of the $^{19}\mathrm{F}(p,\alpha\gamma)^{16}\mathrm{O}$ reaction in the energy range $E_p = 0.8$–3.6 MeV, Z. Phys. A Hadrons Nuclei **357**, 283 (1997).

[29] K. Spyrou, C. Chronidou, S. Harissopulos, S. Kossionides, T. Paradellis, C. Rolfs, W. Schulte, and L. Borucki, Cross section and resonance strength measurements of $^{19}\mathrm{F}(p,\alpha\gamma)^{16}\mathrm{O}$ at $E_p = 200$–800 keV, Eur. Phys. J. A Hadrons Nuclei **7**, 79 (2000).

[30] A. Couture, M. Beard, M. Couder, J. Görres, L. Lamm, P. J. LeBlanc, H. Y. Lee, S. O'Brien, A. Palumbo, E. Stech, E. Strandberg, W. Tan, E. Uberseder, R. Azuma, C. Ugalde, and M. Wiescher, Measurement of the $^{19}\mathrm{F}(p,\gamma)^{20}$Ne reaction and interference terms from $E_{\mathrm{c.m.}} = 200$–760 keV, Phys. Rev. C **77**, 015802 (2008).

[31] I. Lombardo, D. Dell'Aquila, L. Campajola, E. Rosato, G. Spadaccini, and M. Vigilante, Analysis of the $^{19}\mathrm{F}(p,\alpha_0)^{16}\mathrm{O}$ reaction at low energies and the spectroscopy of ^{20}Ne, J. Phys. G: Nucl. Part. Phys. **40**, 125102 (2013).

[32] I. Lombardo, D. Dell'Aquila, A. D. Leva, I. Indelicato, M. L. Cognata, M. L. Commara, A. Ordine, V. Rigato, M. Romoli, E. Rosato, G. Spadaccini, C. Spitaleri, A. Tumino, and M. Vigilante, Toward a reassessment of the $^{19}\mathrm{F}(p,\alpha_0)^{16}\mathrm{O}$ reaction rate at astrophysical temperatures, Phys. Lett. B **748**, 178 (2015).

[33] M. LaCognata, A. M. Mukhamedzhanov, C. Spitaleri, I. Indelicato, M. Aliotta, V. Burjan, S. Cherubini, A. Coc, M. Gulino, Z. Hons, G. G. Kiss, V. Kroha, L. Lamia, J. Mrázek, S. Palmerini, Š. Piskoř, R. G. Pizzone, S. M. R. Puglia, G. G. Rapisarda, S. Romano, M. L. Sergi, and A. Tumino, The Fluorine destruction in stars: First experimental study of the $^{19}\mathrm{F}(p,\alpha_0)^{16}\mathrm{O}$ reaction at astrophysical energies, Astrophys. J. **739**, L54 (2011).

[34] M. LaCognata, S. Palmerini, C. Spitaleri, I. Indelicato, A. M. Mukhamedzhanov, I. Lombardo, and O. Trippella, Updated THM astrophysical factor of the $^{19}\mathrm{F}(p,\alpha)^{16}\mathrm{O}$ reaction and influence of new direct data at astrophysical energies, Astrophys. J. **805**, 128 (2015).

[35] I. Indelicato, M. L. Cognata, C. Spitaleri, V. Burjan, S. Cherubini, M. Gulino, S. Hayakawa, Z. Hons, V. Kroha, L. Lamia, M. Mazzocco, J. Mrazek, R. G. Pizzone, S. Romano, E. Strano, D. Torresi, and A. Tumino, New improved indirect measurement of the $^{19}\mathrm{F}(p,\alpha)^{16}\mathrm{O}$ reaction at energies of astrophysical relevance, Astrophys. J. **845**, 19 (2017).

[36] K. Subotić, R. Ostogić, and B. Stepanāić, Study of the $^{19}\mathrm{F}(p,\gamma)^{20}$Ne radiative capture reaction from 0.2–1.2 MeV, Nucl. Phys. A **331**, 491 (1979).

[37] G. K. Farney, H. H. Givin, B. D. Kern, and T. M. Hahn, High-energy gamma rays from the proton bombardment of fluorine, Phys. Rev. **97**, 720 (1955).

[38] L. Keszthelyi, I. Berkes, I. Demeter, and I. Fodor, Resonances in $\mathrm{F}^{19} + p$ reactions at 224 and 340 keV proton energies, Nucl. Phys. **29**, 241 (1962).

[39] I. Berkes, I. Dézsi, I. Fodor, and L. Keszthelyi, The resonance at 483 and 597 keV proton energies in $\mathrm{F}^{19} + p$ reactions, Nucl. Phys. **43**, 103 (1963).

[40] R. R. Betts, H. T. Fortune, and R. Middleton, Structure of ^{20}Ne: The $^{19}\mathrm{F}(^3\mathrm{He},d)^{20}$Ne reaction, Phys. Rev. C **11**, 19 (1975).

[41] M. Kious, Détermination de taux de réactions nucléaires conduisant á la nucléosynthèse stellaire du Fluor, Ph.D. thesis, Université de Paris-Sud, 1990.

[42] A. M. Lane and R. G. Thomas, *R*-matrix theory of nuclear reactions, Rev. Mod. Phys. **30**, 257 (1958).

[43] D. Tilley, H. Weller, and C. Cheves, Energy levels of light nuclei $A = 16$–17, Nucl. Phys. A **564**, 1 (1993).

[44] I. Lombardo, D. Dell'Aquila, J.-J. He, G. Spadaccini, and M. Vigilante, New analysis of $p + {}^{19}\mathrm{F}$ reactions at low energies and the spectroscopy of natural-parity states in ^{20}Ne, Phys. Rev. C **100**, 044307 (2019).

[45] D. Dieumegard, B. Maurel, and G. Amsel, Microanalysis of Flourine by nuclear reactions: I. $^{19}\mathrm{F}(p,\alpha_0)^{16}\mathrm{O}$ and $^{19}\mathrm{F}(p,\alpha\gamma)^{16}\mathrm{O}$ reactions, Nucl. Instrum. Methods **168**, 93 (1980).

[46] W. B. McLean, A. Ellett, and J. A. Jacobs, The distribution in angle of the long-range alpha-particles from fluorine bombarded with protons, Phys. Rev. **58**, 500 (1940).

[47] G. Breuer, Messung und Analyse von Winkelverteilung und Wirkungsquerschnitt der Reaktion ^{19}F(p, α_0)^{16}O im Energiebereich 0,4 bis 0,72 MeV, Z. Phys. **154**, 339 (1959).
[48] A. Isoya, H. Ohmura, and T. Momota, The angular distributions of the long-range alpha-particles from the reaction ^{19}F(p, α_0)^{16}O, Nucl. Phys. **7**, 116 (1958).
[49] R. Caracciolo, P. Cuzzocrea, A. D. Rosa, G. Inglima, E. Perillo, M. Sandoli, and G. Spadaccini, The 13.645 MeV state in ^{20}Ne, Lett. Nuovo Cimento **11**, 33 (1974).
[50] S. Devons, G. Goldring, and G. R. Lindsey, Emission of electron-positron pairs from light nuclei I: Monopole transition in ^{16}O, Proc. Phys. Soc. Sec. A **67**, 134 (1954).
[51] S. Devons, M. G. N. Hine, and O. R. Frisch, The angular distribution of γ-radiation from light nuclei I. Experimental, Proc. Roy. Soc. London. Ser. A. Math. Phys. Sci. **199**, 56 (1949).
[52] S. Croft, The absolute yield, angular distribution and resonance widths of the 6.13, 6.92 and 7.12 MeV photons from the 340.5 keV resonance of the ^{19}F(p, $\alpha\gamma$)^{16}O reaction, Nucl. Instrum. Methods Phys. Res. Sec. A: Accel., Spectrom., Detect. Assoc. Equip. **307**, 353 (1991).
[53] T. S. Webb, F. B. Hagedorn, W. A. Fowler, and C. C. Lauritsen, Elastic scattering of protons by ^{19}F, Phys. Rev. **99**, 138 (1955).
[54] D. Tilley, C. Cheves, J. Kelley, S. Raman, and H. Weller, Energy levels of light nuclei, A = 20, Nucl. Phys. A **636**, 249 (1998).
[55] G. Caskey, Natural parity states of ^{20}Ne for 12 $< E_x <$ 15.5 MeV, Phys. Rev. C **31**, 717 (1985).
[56] M. K. Mehta, W. E. Hunt, and R. H. Davis, Scattering of alpha particles by oxygen. II. Bombarding energy range 10 to 19 MeV, Phys. Rev. **160**, 791 (1967).
[57] H. Costantini, R. J. deBoer, R. E. Azuma, M. Couder, J. Görres, J. W. Hammer, P. J. LeBlanc, H. Y. Lee, S. O'Brien, A. Palumbo, E. C. Simpson, E. Stech, W. Tan, E. Uberseder, and M. Wiescher, ^{16}O(α, γ)^{20}Ne S factor: Measurements and R-matrix analysis, Phys. Rev. C **82**, 035802 (2010).
[58] E. Berthoumieux, B. Berthier, C. Moreau, J. Gallien, and A. Raoux, Parameterization of nuclear reactions cross section using R-matrix theory, Nucl. Instrum. Methods Phys. Res. Sec. B: Beam Interact. Mater. Atoms **136-138**, 55 (1998), ion Beam Analysis.
[59] D. K. Nauruzbayev, V. Z. Goldberg, A. K. Nurmukhanbetova, M. S. Golovkov, A. Volya, G. V. Rogachev, and R. E. Tribble, Structure of ^{20}Ne states in resonance ^{16}O +α elastic scattering, Phys. Rev. C **96**, 014322 (2017).
[60] S. Hao, C. Huansheng, T. Jiayong, and Y. Fujia, Evaluation of non-Rutherford cross sections, Nucl. Instrum. Methods Phys. Res. Sec. B: Beam Interact. Mater. Atoms **90**, 593 (1994).
[61] C. M. Laymon, K. D. Brown, and D. P. Balamuth, [^{16}O(0_2^+)+α] parentage of continuum levels in ^{20}Ne, Phys. Rev. C **45**, 576 (1992).
[62] K. L. Laursen, O. S. Kirsebom, H. O. U. Fynbo, A. Jokinen, M. Madurga, K. Riisager, A. Saastamoinen, O. Tengblad, and J. Äystö, High-statistics measurement of the β-delayed α spectrum of ^{20}Na, Eur. Phys. J. A **49**, 79 (2013).
[63] W. Huang, X. Xu, R. Ma, Z. Hu, J. Guo, Y. Guo, H. Liu, and L. Xu, Decay study of ^{20}Na and its beta-delayed ^{16}O recoiling, Sci. China Ser. A: Math. **40**, 638 (1997).
[64] R. E. Azuma, E. Uberseder, E. C. Simpson, C. R. Brune, H. Costantini, R. J. de Boer, J. Görres, M. Heil, P. J. LeBlanc, C. Ugalde, and M. Wiescher, AZURE: An R-matrix code for nuclear astrophysics, Phys. Rev. C **81**, 045805 (2010).
[65] E. Uberseder and R. J. deBoer, `AZURE2` *User Manual* (2015), azure.nd.edu.
[66] C. R. Brune, Alternative parametrization of R-matrix theory, Phys. Rev. C **66**, 044611 (2002).
[67] C. R. Brune and R. J. deBoer, Secondary γ-ray decays from the partial-wave T matrix with an R-matrix application to ^{15}N(p, $\alpha_1\gamma$)^{12}C, Phys. Rev. C **102**, 024628 (2020).
[68] G. Audi, A. Wapstra, and C. Thibault, The Ame2003 atomic mass evaluation: (II). Tables, graphs and references, Nucl. Phys. A **729**, 337 (2003).
[69] J.-J. He, I. Lombardo, D. Dell'Aquila, Y. Xu, L.-Y. Zhang, and W.-P. Liu, Thermonuclear ^{19}F(p, α_0)^{16}O reaction rate, Chin. Phys. C **42**, 015001 (2018).
[70] H. W. Becker, W. E. Kieser, C. Rolfs, H. P. Trautvetter, and M. Wiescher, Resonance strengths of some light nuclei, Zeitschrift für Physik A Atoms and Nuclei **305**, 319 (1982).
[71] R. M. Sinclaii, Gamma radiation from certain nuclear reactions, Phys. Rev. **93**, 1082 (1954).
[72] T. W. Bonner and J. E. Evans, Resonances in the disintegration of fluorine and lithium by protons, Phys. Rev. **73**, 666 (1948).
[73] C. Y. Chao, A. V. Tollestrup, W. A. Fowler, and C. C. Lauritsen, Low-energy alpha-particles from fluorine bombarded by protons, Phys. Rev. **79**, 108 (1950).
[74] D. Zahnow, C. Angulo, C. Rolfs, S. Schmidt, W. H. Schulte, and E. Somorjai, The $S(E)$ factor of ^{7}Li(p, γ)^{8}Be and consequences for $S(E)$ extrapolation in ^{7}Be(p, γ_0)^{8}B, Z. Physik A Hadrons Nuclei **351**, 229 (1995).
[75] D. Ezer and A. G. W. Cameron, The evolution of hydrogen-helium stars, Astrophys. Space Sci. **14**, 399 (1971).
[76] R. H. Cyburt, B. D. Fields, K. A. Olive, and T.-H. Yeh, Big bang nucleosynthesis: Present status, Rev. Mod. Phys. **88**, 015004 (2016).
[77] M. Pignatari, F. Herwig, R. Hirschi, M. Bennett, G. Rockefeller, C. Fryer, F. X. Timmes, C. Ritter, A. Heger, S. Jones, U. Battino, A. Dotter, R. Trappitsch, S. Diehl, U. Frischknecht, A. Hungerford, G. Magkotsios, C. Travaglio, and P. Young, NuGrid stellar data set. I.stellar yields from H to Bi for stars with metallicities $Z = 0.02$ and $Z = 0.01$, Astrophys. J. Suppl. Ser. **225**, 24 (2016).
[78] R. H. Cyburt, A. M. Amthor, R. Ferguson, Z. Meisel, K. Smith, S. Warren, A. Heger, R. D. Hoffman, T. Rauscher, A. Sakharuk, H. Schatz, F. K. Thielemann, and M. Wiescher, The JINA REACLIB database: Its recent updates and impact on type-I x-ray bursts, Astrophys. J. Suppl. **189**, 240 (2010).
[79] M. Limongi and A. Chieffi, Presupernova evolution and explosive nucleosynthesis of zero metal massive stars, Astrophys. J. Suppl. **199**, 38 (2012).
[80] https://astrohub.uvic.ca.
[81] http://csa.phys.uvic.ca.

Correction: The title contained a minor misprint and has been fixed. The second entry in the fourth column contained an error and has been repaired.